

Hydrodynamical Description of 200 A GeV/c S+Au Collisions: Hadron and Electromagnetic Spectra

Josef Sollfrank

Research Institute for Theoretical Physics, University of Helsinki, Finland

Pasi Huovinen, Markku Kataja, P.V. Ruuskanen

Department of Physics, University of Jyväskylä, Finland

Madappa Prakash

Physics Department, SUNY at Stony Brook, Stony Brook, USA

Raju Venugopalan

National Institute for Nuclear Theory, University of Washington, Seattle, USA

(March 24, 2018)

Abstract

We study relativistic S+Au collisions at 200A GeV/c using a hydrodynamical approach. We test various equations of state (EOSs), which are used to describe the strongly interacting matter at densities attainable in the CERN-SPS heavy ion experiments. For each EOS, suitable initial conditions can be determined to reproduce the experimental hadron spectra; this emphasizes the ambiguity between the initial conditions and the EOS in such an approach. Simultaneously, we calculate the resulting thermal photon and di-electron spectra, and compare with experiments. If one allows the excitation of resonance states with increasing temperature, the electro-magnetic signals

from scenarios with and without phase transition are very similar and are not resolvable within the current experimental resolution. Only EOSs with a few degrees of freedom up to very high temperatures can be ruled out presently. We deduce an upper bound of about 250 MeV for the initial temperature from the single photon spectra of WA80. With regard to the CERES dilepton data, none of the EOSs considered, in conjunction with the standard leading order dilepton rates, succeed in reproducing the observed excess of dileptons below the ρ peak. Our work, however, suggests that an improved measurement of the photon and dilepton spectra has the potential to strongly constrain the EOS.

PACS numbers: 25.70.np, 12.38.Mh, 12.40.Ee, 47.75.+f

I. INTRODUCTION

The use of hydrodynamics for simulations of nuclear collisions has a long tradition [1–3]. If applicable, hydrodynamics has some advantages over the more fundamental kinetic calculations, which are usually performed as Monte-Carlo simulations. Besides its relative simplicity, the use of familiar concepts such as temperature, flow velocity, energy density, pressure, etc. leads to an intuitively transparent picture of the space-time evolution of the system. Another great advantage is the direct use of the equation of state (EOS) of strongly interacting matter. Testing different EOSs by comparing with experiments should give us more insight into the behavior of nuclear matter under extreme conditions of temperature and/or density. This is important, since one of the main reasons to study high energy heavy ion collisions is to confirm the possible phase transition from hadronic matter to the quark-gluon plasma (QGP) [4]. The necessary energy densities are estimated to be around 1–2 GeV/fm³, presently experimentally available at the Brookhaven AGS and the CERN-SPS. Of these two facilities, conditions to observe signals of the phase transition are more favorable at the CERN-SPS, because of the higher incident momenta of the nuclei.

In this work, we analyze the data from the heavy ion experiments at the CERN-SPS with 200A GeV/*c* incident momentum [5]– [14], concentrating on the S + Au system. For this system, yields of both the hadronic and electromagnetic (dileptons and photons) probes are now available. A hydrodynamical treatment of the nuclear collisions in this energy range is not new [15]– [19], but the large set of new and updated experimental data allows us to achieve a deeper insight into the space-time evolution of these reactions.

Our emphasis here is on the simultaneous description of the hadron and electromagnetic data. Since hadrons interact throughout the dense phase of the collision, the hadronic spectra are chiefly determined from the conditions at the freeze-out of matter. However, different initial conditions combined with different EOSs can lead to the same final particle distributions. In contrast, photon and lepton pairs are emitted throughout the dense stage

and escape without interactions. The measured spectra thus probe the different temperature and flow conditions during the evolution. These should have a different dependence on the initial conditions and on the EOS, in comparison to the hadron spectra. This may help to further reduce the ambiguity in the initial conditions and uncertainties in the EOS.

Our hydrodynamical calculations assume azimuthal symmetry around the beam axis. Thus, we simulate only central collisions with impact parameters close to zero. We do not describe the production of matter within hydrodynamics, but start the calculation at an initial time when the system is likely to have reached thermal and chemical equilibrium. We explore different initial conditions, taking guidance from the experimental data (where available) on particle production in proton-proton ($p + p$) collisions in choosing what could be considered as a realistic initial state. However, one must be aware that nuclear effects are likely already present at the production stage, and the initial conditions cannot be uniquely determined from $p + p$ processes alone.

A major concern is the uncertainty in the nuclear EOS. It is experimentally and theoretically well known only around the ground state of nuclear matter. At higher temperatures and densities, model predictions are widely different. The main goal in this study is to derive constraints on the EOS by comparing the hydrodynamical calculations with hadronic and electromagnetic data simultaneously from S + Au collisions at $200A$ GeV/ c .

The paper is organized as follows: In Sec II, we briefly introduce the hydrodynamical equations and address some problems which arise when seeking numerical solutions of these equations. In Sec. III, the different EOSs explored are described. The initial conditions are discussed in Sec. IV. In Secs. V, VI and VII, we describe the calculation of the final hadron, photon, and dilepton spectra, respectively. Results are discussed in Sec. VIII, and our conclusions are given in Sec. IX. In the appendix, we briefly explain how we incorporated the CERES kinematic cuts and the detector resolution.

II. THE HYDRODYNAMICAL EQUATIONS

The basic equations of hydrodynamics are the local conservation of energy and momentum, which in Lorentz-covariant form are written as

$$\partial_\mu T^{\mu\nu}(x) = 0. \quad (1)$$

We use the ideal fluid ansatz for the energy-momentum tensor

$$T^{\mu\nu}(x) = [\varepsilon(x) + p(x)]u^\mu(x)u^\nu(x) - p(x)g^{\mu\nu}, \quad (2)$$

where $\varepsilon(x)$ is the local energy density, $p(x)$ is the local pressure, and $u^\mu(x)$ is the local four-velocity, normalized to $u^\mu u_\mu = 1$. In principle, viscous effects may be included, but would lead to a major increase in the numerical effort [3,20]. However, the calculation generates some numerical viscosity, as explained below.

We include finite baryon density, ρ_B , in our system and express baryon number conservation locally in the form

$$\partial_\mu j_B^\mu = 0, \quad (3)$$

in terms of the baryon current $j_B^\mu = \rho_B u^\mu$.

Using the definition Eq. (2), the continuity Eqs. (1) and (3) can be written more explicitly as

$$\begin{aligned} \partial_t T^{00} + \vec{\nabla} \cdot (T^{00} \vec{v}) &= -\vec{\nabla} \cdot (p \vec{v}), \\ \partial_t T^{0i} + \vec{\nabla} \cdot (T^{0i} \vec{v}) &= -\partial_i p, \\ \partial_t j_B^0 + \vec{\nabla} \cdot (j_B^0 \vec{v}) &= 0. \end{aligned} \quad (4)$$

In order to solve Eq. (4), one additional input is needed, namely, the equation of state (EOS). The EOS relates the pressure $p = p(\varepsilon, \rho_B)$ to the energy and baryon densities. The different choices of the EOS are described in the next section.

The partial (hyperbolic) differential equations, Eq. (4), are solved numerically on a computer using a finite difference method. We use the SHASTA algorithm [21] in two spatial

dimensions, radial and longitudinal. Some details of implementing this algorithm are explained in the appendix of Ref. [20]. However, there are two essential modifications. Firstly, since we now have a problem with two spatial dimensions [22], the flux correction must be modified accordingly, as described in Ref. [23]. Secondly, the flux correction involves a parameter η [20,24], the anti-diffusive constant, which regulates the residual numerical anti-diffusive flux in the algorithm. Theoretically, for $\eta = 1/8$, diffusion vanishes almost completely, leading, however, to the appearance of ripples in the presence of steep gradients.

On the other hand, a residual diffusive flux mimics viscosity in the calculation, since it generates entropy in the system. In Ref. [20], a large residual diffusive flux was allowed by choosing a small value for the anti-diffusive constant, $\eta = 0.08$. This value was determined by trying to create as much entropy as is maximally allowed in the rarefaction wave, typically $\lesssim 10\%$. However, it turns out that the flux across the freeze-out surface (Eq. (27) below) now has two contributions; the normal convective part and the diffusive part. Because we cannot assign a velocity to the numerical diffusive flux, it cannot be converted into particle spectra at the freeze-out surface. Therefore, we diminish the diffusive flux by setting $\eta = 0.11$, as suggested also in Ref. [24], and neglect the small residual diffusive flux across the freeze-out hypersurface. This leads to a small, of order $\lesssim 5\%$, loss in the baryon number and total energy across the freeze-out hypersurface. (The stability of the numerical calculation increases as η is diminished from the limiting value $1/8 = 0.125$. Our choice, $\eta = 0.11$, is a compromise between numerical stability and the diffusive loss across the freeze-out surface.) The value of η has a small influence on the space-time evolution, a larger diffusive flux leading to a more rapid cooling of the system. This has only a small effect, especially on the electromagnetic spectra.

At the moment, our numerical code assumes a mirror symmetry in the longitudinal direction with respect to the center of mass ($f(z) = f(-z)$ for scalar quantities). This is a very good approximation for symmetric colliding systems. However, we apply it here to the

asymmetric S + Au collisions. Thus, we are presently unable to reproduce the asymmetry in the rapidity distributions of hadrons, which is observed in experiment. However, in the central rapidity region, where most of the experimental data are measured, we do not expect this to affect significantly the transverse spectra or the electromagnetic yields. We will consider the longitudinal asymmetry in a later work.

III. THE EQUATION OF STATE

The equation of state (EOS) in the energy density domain of $\varepsilon \gtrsim 1 \text{ GeV}/\text{fm}^3$ or baryon density $\rho_B \gtrsim 2\rho_0$, where ρ_0 is the density of ground state nuclear matter, is theoretically quite uncertain. At the CERN-SPS energies, the relevant energy densities are not high enough that the well established techniques of finite temperature *perturbative* QCD will apply. At the same time, the energy densities are typically too high for low energy approaches, such as chiral perturbation theory, to be applicable. Hadronic and quark–gluon matter at these temperatures and densities, and especially the chiral and/or de-confinement transitions between the two phases at some critical temperature and density, are non-perturbative phenomena which are currently investigated through lattice simulations of QCD.

Simulations of pure SU(3) gauge theory indicate the occurrence of a first-order deconfinement transition around $T_c \simeq 260 \text{ MeV}$ through studies of hysteresis, co-existing states, and abrupt quantitative changes in the various thermodynamic functions. Recent simulations on larger lattices ($16^3 \times 32$) suggest that finite size effects are reasonably well understood for pure glue — an estimate for the critical energy density for pure SU(3) is $\sim 1 \text{ GeV}/\text{fm}^3$ [25]. For full lattice QCD with dynamical quarks, the situation is less clear, particularly in the critical region. However, a recent calculation [26] shows that the energy density displays a rapid change in a narrow region around $T_c \simeq 150 \text{ MeV}$, while the pressure changes more smoothly.

Though the present uncertainties preclude a quantitative description of the thermody-

dynamic functions around the critical region, one may observe i) a smooth crossover between hadronic matter and the quark gluon phase and ii) a sizable and rapid change in the entropy density. These features may be roughly reproduced in a two phase description of the transition. Indeed, even if the transition were a *sharp* first order transition, it is unlikely that the hydrodynamic flow simulations would be extremely sensitive to the width (in temperature) of the critical region [27]. Therefore, for the purpose of our hydrodynamic simulations, we will construct EOSs for both the hadron and quark gluon state variables and match them at the critical boundary in temperature and chemical potential by a Maxwell construction. In practice, when implemented in simulations, this boundary is smoothed over using a hyperbolic tangent profile of width Δ . It has been checked that the results of our simulations are insensitive to Δ , as long as $\Delta/T_c \ll 1$ [28]. In addition to studying EOSs with a sharp cross over (but differing critical temperatures and latent heat), we will also consider an EOS with purely hadronic degrees of freedom.

Let us first discuss the EOS we use for the hadronic phase. For a dilute hadronic gas at temperatures well below the pion mass, state variables can be computed reliably using a virial expansion with input from empirical scattering cross sections [29,30]. It was observed that the state variables for an interacting hadron gas are well approximated by those for a Boltzmann gas of free hadrons and resonances. At temperatures comparable to the pion mass or higher, third and higher virial coefficients are important. Presently, there is no reliable way to compute these. For want of a systematic prescription, we shall stretch our conclusions from the virial expansion approach and assume that a dense hadron gas is roughly approximated by a gas of free hadrons and resonances.

We restrict our studies here to a hadron gas, which contains the following hadrons with their corresponding anti-particles:

$$\pi, K, \eta, \rho, \omega, K^*, p, n, \eta', \phi, \Lambda, \Sigma, \Delta, a_1, \Xi, \Sigma(1385). \quad (5)$$

Beside stable particles (on strong interaction time scales), the hadron gas also contains

resonance states. This should mimic the attractive interaction among the hadrons in the spirit of the bootstrap model of Hagedorn [31], although we keep the number of resonance states finite. If we assume a phase transition to the QGP at temperatures around $T_c \approx 150$ MeV, then the limited number of hadronic states is justified, because of the suppression of higher mass states through the Boltzmann factor.

As mentioned above, we will also consider a pure hadronic EOS, which does not exhibit a phase transition. In this case, somewhat higher temperatures are encountered in our calculations. Therefore, a sensitivity on the upper mass cut in the hadronic mass spectrum could be expected. We expect this to show up more in the values of the temperature rather than in the evolution of the flow. While hadronic spectra are not very sensitive to this cut, electromagnetic rates, however, could decrease. On the other hand, for consistency, we should include the increase in electromagnetic emission from processes involving the heavy resonances. To some extent, these effects tend to cancel each other. Mainly due to the numerical limitations of our hydrodynamical simulations, we have included only those states listed above, even at high temperatures.

In order to derive the EOS, we begin with the grand canonical partition function for a non-interacting resonance gas. It is given by

$$\mathcal{Z}^H(T, V, \mu_B, \mu_S) = \prod_h \exp [Z_h(T, V, \mu_h)] , \quad (6)$$

where V is the volume, and the product is over the different hadron species h . The chemical potential μ_h of the hadron h is given by its baryon number B_h and its strangeness S_h through

$$\mu_h = B_h \mu_B + S_h \mu_S \quad (7)$$

in full chemical equilibrium. We will use this assumption throughout the expansion, although there are indications of deviations, especially for the strange particles [32]. The partition function Eq. (6) is, in general, a function of four unknown variables. For calculations of intensive variables, the volume cancels and the value of the strangeness chemical potential

μ_S can be related to T and μ_B by the requirement of local strangeness neutrality.

The partition function $Z_h(T, V, \mu_h)$ for hadron species h is

$$\ln Z_h(T, V, \mu_h) = \beta V p_h = \frac{g_h \beta V}{6\pi^2} \int_{m_h}^{\infty} dE \frac{(E^2 - m_h^2)^{3/2}}{e^{\beta(E - \mu_h)} \pm 1}, \quad (8)$$

where g_h is the degeneracy factor, m_h is the mass, and μ_h is the chemical potential of hadron h . The \pm sign corresponds to fermions and bosons, respectively. From the partition function Eq. (6), we can calculate all thermodynamical quantities. Specifically, we have

$$\rho_B(T, \mu_B) = \frac{T}{V} \frac{\partial \ln \mathcal{Z}^H}{\partial \mu_B} \quad (9)$$

$$\varepsilon(T, \mu_B) = \frac{1}{V} \frac{\partial \ln \mathcal{Z}^H}{\partial \beta} \quad (10)$$

$$p(T, \mu_B) = T \frac{\partial \ln \mathcal{Z}^H}{\partial V} = \frac{T}{V} \ln \mathcal{Z}^H. \quad (11)$$

From these equations, the pressure can be solved as a function of the energy density ε and the baryon density ρ_B . This form of the EOS, $p = p(\varepsilon, \rho_B)$, is needed in solving the hydrodynamic equations and in practice is obtained numerically from Eqs. (10) and (11).

In the limit of high baryon densities, the repulsive interactions between particles have to be taken into account. Otherwise, the hadronic phase is preferred over the quark-gluon phase. At the temperatures of interest, repulsive interactions reduce the contributions from the high mass part of the spectrum [33], justifying our use of a finite number of resonance states in the EOS. It has been shown [30] that within the different ways to include repulsion, a mean field approach, such as in Ref. [34], gives the most realistic results. Thus, we will introduce a repulsive mean field potential \mathcal{V} , which we couple only to the net baryon density. This is similar in spirit to the Walecka model [35]. By including many of the resonance states, the main attractive interactions (akin to the scalar interactions of the Walecka model) are already taken into account.

We assume that the repulsive potential energy density \mathcal{V} is a function of ρ_B of the form

$$\mathcal{V}(\rho_B) = \frac{1}{2} K \rho_B^2, \quad (12)$$

where K is the mean field repulsion parameter. The partition function \mathcal{Z}^{MF} with a mean field interaction Eq. (12) is given by [36]

$$\mathcal{Z}^{\text{MF}} = \exp \{-\beta V[\mathcal{V}(\rho_B) - \rho_B \mathcal{V}'(\rho_B)]\} \prod_h \exp [Z_h(T, V, \mu_B^{\text{eff}}, \mu_S)] , \quad (13)$$

where the effective baryon chemical potential

$$\mu_B^{\text{eff}} = \mu_B - \mathcal{V}'(\rho_B) = \mu_B - K \rho_B \quad (14)$$

describes the shift in the particle energy by $K \rho_B$ due to the repulsive interaction. Using Eq. (9) with Eq. (13) leads to a self-consistency equation for the baryon density

$$\rho_B = \sum_b \int d^3p \frac{1}{\exp [(E - \mu_B B_b + K \rho_B - \mu_S S_b)/T] + 1} . \quad (15)$$

Once ρ_B is solved, applying Eqs. (10) and (11) to the mean field partition function, Eq. (13), gives the repulsion corrected energy density and pressure. The resulting EOS is labeled as EOS H and has one free parameter K . The ideal gas equation of state $p(\varepsilon, \rho_B) = \varepsilon/3$, valid for massless non-interacting particles, is referred to as EOS I. We use this with three massless pions, to illustrate the effect of the number of hadronic degrees of freedom.

So far, we have considered the equation of state using only the hadronic degrees of freedom. We will now construct an EOS having a phase transition to the QGP. As discussed earlier, the QGP in the critical region is highly nonperturbative and is best understood from QCD lattice simulations. For simplicity, the results of these simulations can be parametrized in terms of an ideal massless parton gas. In terms of temperature T and chemical potential μ_B , the thermodynamic densities are given by

$$p = \frac{(32 + 21N_f)\pi^2}{180} T^4 + \frac{N_f}{2} \mu_q^2 T^2 + \frac{N_f}{4\pi^2} \mu_q^4 - B \quad (16)$$

$$\varepsilon = 3p + 4B \quad (17)$$

$$\rho_B = N_f \mu_q^2 T + \frac{N_f}{\pi^2} \mu_q^3 , \quad (18)$$

where $\mu_q = \mu_B/3$. B is the bag constant, and we use the number of flavors $N_f = 2.5$ in order to simulate effects of the finite strange quark mass.

The phase boundary is determined by the pressure balance, $p_{\text{HG}} = p_{\text{QGP}}$, between the two phases at equilibrium. In the mixed phase, ε and ρ_B are calculated using the Maxwell construction. We define

$$w(\varepsilon, \rho_B) = \frac{V^{\text{QGP}}}{V^{\text{HG}} + V^{\text{QGP}}} \quad ; \quad 0 \leq w \leq 1 \quad (19)$$

as the volume fraction of the QGP in the mixed phase.

The resulting EOS depends on two parameters, the mean field repulsion parameter K and the bag constant B . In this work, we give results for only two different choices of K and B , and call these parametrizations EOS A and EOS B. The two parameter sets are chosen to resemble the known features of the phase transition from lattice calculations [26], the difference encompassing the uncertainty of lattice results. These indicate a value $T_c \approx 140 - 160$ MeV for the transition temperature and $\Delta\varepsilon \approx 1 - 1.5$ GeV/fm³ for the latent heat. Our EOS A, given by $K = 450$ MeV fm³ and $B^{1/4} = 235$ MeV, is similar to the one used in Ref. [37]. The resulting T_c is 165 MeV, and $\Delta\varepsilon = 1.4$ GeV/fm³. For EOS B, the parameters are $K = 660$ MeV fm³ and $B^{1/4} = 200$ MeV, resulting in $T_c = 140$ MeV and $\Delta\varepsilon = 0.8$ GeV/fm³. This parametrization should represent reasonable lower bounds for T_c , μ_c , and the latent heat. The parameters for the EOSs we use are summarized in Table I.

The phase diagrams of equations of state A and B are shown in Fig. 1. The difference in the latent heat can be seen if one plots the phase boundaries in the $\rho_B - \varepsilon$ plane. This can be read off from Fig. 2, where the pressure is shown as a function of ρ_B and ε . For the EOS A, there is a large increase in the pressure, even in the mixed phase, with increasing baryon density, while for the EOS B the increase is much smaller. It would be interesting to obtain from hydrodynamical calculations constraints on the EOS at finite baryon density, since nothing is known so far from lattice calculations in this region. Presently, however,

the large uncertainties in the initial conditions preclude definitive conclusions to be drawn.

IV. THE INITIAL CONDITIONS

Hydrodynamical simulations at energies near or below 10 A GeV (BEVALAC and AGS) usually start with the colliding nuclei before the impact and include the initial compression and particle production. In the one-fluid hydrodynamics, the nuclei fuse to a single fluid, implying, at zero impact parameter, a complete stopping of equal size nuclei. At higher energies, as at the CERN-SPS, RHIC and LHC, this is not justified, and one must be able to incorporate nuclear transparency in the description. Instead of trying to describe the production and equilibration within hydrodynamics, we start the calculation from initial conditions which specify the hydrodynamic state of the system at time t_0 . Initial conditions parametrize the production and equilibration dynamics. Note that t_0 only plays the role of a bookkeeping device in the numerical calculations. Thermalization time does not enter explicitly in the parametrization, but, physically, it may be related to the initial longitudinal size, z_0 , at thermalization. In some cases, we find it useful to relate z_0 with t_0 when defining the initial longitudinal velocity profile.

Physically, the uncertainty in the initial conditions arises mainly from the lack of definitive knowledge about the nuclear stopping power and the time scale for equilibration. Two extreme scenarios are the full stopping model of Landau [1] and the full scaling expansion model espoused by Bjorken [38], in which $v_z = z/t$, beginning with equilibration. Although the precise energies at which these extreme cases are practically useful is unknown, the first case is expected to apply at moderately high energies and the second at ultrarelativistic energies. Since the present experiments fall between these limits, we have developed parametrizations which span the range between these two extremes. We will try to incorporate some known features of hadron-hadron collisions in the parametrization, which are also

constrained to satisfy the conservation of energy and baryon number.

We first consider the initial velocities. The collective four velocity is denoted by $u^\mu = \gamma(1, \vec{v})$, where \vec{v} is the flow velocity vector. Since we consider zero impact parameter cylindrically symmetric collisions only, we do not expect significant collective motion initially, and take the velocity in the radial direction at t_0 to vanish, i.e., $\vec{v}_r(t_0, r) = 0$. Note that for the Landau initial conditions, the initial longitudinal velocity also vanishes, i.e., $v_z(t_0, r, z) = 0$. Strictly speaking, the Bjorken model applies only in the infinite energy limit. In this case, the scaling ansatz for the four velocity is

$$u^\mu(z, t) = \frac{1}{\tau}(t, 0, 0, z), \quad (20)$$

implying $v_z = z/t$. Invariance under longitudinal Lorentz boosts means that the thermodynamic quantities depend only on the longitudinal proper time $\tau = \sqrt{t^2 - z^2}$, which equals the local time in the rest frame of any fluid element.

At finite, albeit high collision energies, the longitudinal extent of the system is finite and the Bjorken scenario does not work properly in the fragmentation regions. Since we perform the numerical calculation using variables in the center-of-mass frame of the participating nucleons, we specify the initial condition at a fixed time t_0 in this frame. We choose an initial velocity profile of the following form:

$$v_z(z) = \tanh(z/t_0), \quad y(z) = z/t_0. \quad (21)$$

In this form, t_0 should be regarded as a constant, which fixes the rapidity of produced matter at the edge z_0 , rather than the equilibration time.

The reason for taking the rapidity y , instead of velocity v_z , to be proportional to z is purely practical. For numerical calculations, initial conditions must be smoothed and extended over the edge of the produced matter, initially at z_0 . The above parametrization leads to the Bjorken limit, Eq. (20), in the inner part ($z/t_0 \ll 1$), and extrapolates the

velocity smoothly to unity in the outer parts, where the thermodynamic densities approach zero.

The energy density distribution in the Bjorken model is constant along contours of equal proper time $\tau_0(t, z) = \sqrt{t^2 - z^2}$. However, in the global frame, at fixed time $t = t_0$, it scales with z as ($\varepsilon_0 := \varepsilon(t_0, 0)$) [38]

$$\frac{\varepsilon(t_0, z)}{\varepsilon_0} = \left(\frac{t_0}{\sqrt{t_0^2 - z^2}} \right)^{4/3} = \gamma(z)^{4/3}, \quad (22)$$

if an ideal gas EOS, $\varepsilon = 3p$, is assumed. In the last term, $\gamma(z) = (1 - (z/t_0)^2)^{-1/2}$ is the relativistic γ -factor for the Bjorken expansion velocity, Eq. (20).

We use Eq. (22) for our initial parametrization, despite the fact that it is strictly valid only for the velocity field Eq. (20), i.e., the Bjorken picture. One factor of γ in this equation expresses the time dilatation effect for the moving cells and the factor $\gamma^{1/3}$ the energy loss due to the work done by pressure in the expansion. Retaining this factor whenever the initial longitudinal velocity is non-vanishing is therefore physically well motivated. Then the remaining factor in $\varepsilon(t_0, z)$ represents the energy density in the local rest frame, and values at different z have the same physical interpretation. In the Bjorken picture, a rapidity plateau indicates constant local energy density. At fixed global initial time, this leads to increasing $\varepsilon(t_0, z)$ with increasing z . Since, at finite collision energy, the thermodynamic densities vanish when $z > z_0$, this constraint will ensure that the energy density will have a maximum at finite z . This is in contrast to Ref. [18], in which the authors employed a constant energy density along z until the edges are reached.

In production processes, distributions are always cut off smoothly when the phase space boundary is approached. Smoothing also helps to avoid oscillations in the numerical calculations. We implement smoothing by multiplying the distributions with a Fermi function

$$f(x, x_0, a_x) = \frac{1}{\exp[(|x| - x_0)/a_x] + 1}, \quad (23)$$

where a_x , $x = r, z$ is the diffuseness parameter in the radial and the longitudinal directions, respectively. The initial energy distribution is then given by

$$\varepsilon(z, r) = \varepsilon_0 \gamma(z)^{4/3} f(z, z_0, a_z) f(r, r_0, a_r). \quad (24)$$

Since our code is symmetric in z in the center-of-mass frame of the participant nucleons, or equivalently, of the produced fireball, we cannot reproduce the asymmetric shape of rapidity distributions in S+Au collisions. In the central region, $y = 0$, we expect effects from the asymmetry on the expansion dynamics to be less important than those from the average longitudinal gradients, which are properly accounted for in the code.

In the case of the longitudinal scaling expansion, the rapidity density of baryon number, dN_B/dy does not change during the expansion. This allows us to relate the rapidity density to the initial baryon density through the equation

$$\rho_B(z) = \frac{1}{\pi R_{\text{proj}}^2 dz \gamma(z)} \frac{dN_B}{dy} \frac{dy}{dz} dz = \frac{1}{\pi R_{\text{proj}}^2 \tau} \frac{dN_B}{dy} \left[\frac{\tau}{\gamma(z)} \frac{dy}{dz} \right], \quad (25)$$

where, for the scaling expansion, the expression in square brackets equals unity. In our case, expansion modifies the rapidity distributions and the problem is to find a reasonable choice for the initial dN_B/dy .

In nucleon-nucleon collisions, the leading particle effect in the nucleon distributions causes more nucleons to be present in the fragmentation regions than at central rapidity [39,40]. In nuclear collisions, however, more stopping is present and it depends on the mass numbers of the colliding nuclei. Here, we assume that the initial rapidity density of baryons is flat, implying constant density at constant proper time in the Bjorken parametrization. At fixed global time, the baryon distribution as a function of z is then

$$\rho_B(z) = b_0 \gamma(z) f(z, z_0, a_z) f(r, r_0, a_r), \quad (26)$$

where b_0 is the central baryon density.

Some of the initial parameters can be fixed by geometry. A natural choice for r_0 is the

sulphur radius, 3.65 fm. For the diffuseness parameter in a Woods-Saxon [41] parametrization of the nuclear surface, we take the value $a_r = 0.5$ fm. We set $a_z = 0.13$ fm in order to have $a_r/r_0 \approx a_z/z_0$. The number of participating nucleons is calculated from geometry, by assuming that at impact parameter zero the sulphur nucleus coalesces with a central tube of the gold nucleus having the diameter of sulphur. From the calculated value $B_{\text{tot}} = 104$, we obtain the rapidity of the cm frame of the participating nucleons, $y_{\text{cm}} = 2.6$, and the total cm energy, $E_{\text{tot}} = 970$ GeV. This total energy should be considered to give the overall scale of the energy in the fireball, since small changes in the rapidity distributions of final particles in the fragmentation regions easily cause 10-20% changes in the total energy. We do not consider such deviations to be significant when fitting the pion spectra. Given E_{tot} and B_{tot} , we can fix two of the remaining five parameters in the initial conditions. These are the central initial energy density ε_0 and baryon density b_0 .

The real ambiguity in the initial condition lies in the parameters z_0 and t_0 . While in the Bjorken scenario, they are related through $t_0 = z_0/c$, i.e., the edge of matter is by definition on the light cone; this does not hold in a finite energy scenario, like the one introduced here. Now, the initial longitudinal velocity can deviate from the scaling behavior, $v_{z,\text{sc}} = z/t$, and with our parametrization, Eq. (21), fixing t_0 is equivalent to fixing y_0 , the rapidity at z_0 , as is done also in Refs. [15,18].

The values of z_0 and t_0 are chosen to fit the pion spectra. In Fig. 3, we show the initial profiles for the calculation with the EOS A. The main features are the maximum of the energy density at finite z instead of at $z = 0$, and a smooth behavior instead of a discontinuous one at the edge of matter. During the calculation, the velocity of the first vacuum cell is set equal to the velocity of the nearest cell containing matter.

The profiles of the energy density for the other EOSs look similar. The parameters are listed in Table II. In calculating the total energy and the baryon number of the initial matter, only the volume with $\varepsilon(\vec{x}) > \varepsilon_f$ (ε_f is the freeze-out energy density) is included in

the integration. The results are equal to the total energy and baryon number fluxes through the freeze-out surface.

V. FREEZE-OUT

We define the freeze-out surface as the space-time hypersurface σ_μ of constant energy density. The value of ε_f is chosen in such a way that the mean value of the temperature on σ_μ is $T_f \simeq 140$ MeV. This value for the temperature is chosen on the basis of calculations comparing the various mean free paths of the hadrons in the system with the size of the fireball [42–45].

The hadron spectra are calculated by assuming thermal momentum distributions and chemical equilibrium on the freeze-out surface. The invariant momentum distribution of a hadron h is then given by [46]

$$E \frac{dN}{d^3p} = \frac{g_h}{(2\pi)^3} \int_{\sigma} d\sigma_\mu p^\mu \frac{1}{\exp[(p_\nu u^\nu - \mu)/T_f] \pm 1}, \quad (27)$$

where the temperature $T_f(x)$, the chemical potential $\mu(x)$, and the fluid flow four-velocity $u^\nu(x)$ are determined on the surface σ_μ from the hydrodynamic calculation. After calculating the momentum distribution for each hadron included in the EOS, Eq. (5), the contributions from unstable resonance decays are added to the stable hadron spectra. We use the approximations and decay kinematics described in Ref. [47]. Finally, we integrate over the experimental acceptance in p_T and y .

VI. PHOTONS

The thermal emission rate for photons can be shown to be directly proportional to the trace of the retarded photon self energy at finite temperature [48]. In the QGP, the imaginary parts of the lowest order contributions to the self energy correspond to tree level QCD Compton and annihilation diagrams, $q\bar{q} \rightarrow g\gamma$, $q(\bar{q})g \rightarrow q(\bar{q})\gamma$, respectively. Contributions

from these diagrams alone are infrared divergent. However, it has been shown by Braaten and Pisarski [49] that these long range effects are screened at finite temperature. The above mentioned diagrams were calculated, including the Braaten–Pisarski resummation, in Ref. [50,51] for zero baryon chemical potential. This result was extended in Ref. [52] to finite baryon density. We use the results of Ref. [52], since we have finite baryon density explicitly in our calculation. However, the influence of the term containing the chemical potential is small. For two quark flavors, the rate is [52]

$$E_\gamma \frac{dR^{\text{QGP}}}{d^3p} = \frac{5}{9} \frac{\alpha \alpha_s T^2}{2\pi^2} \left(1 + \frac{\mu_q^2}{\pi^2 T^2} \right) e^{-E_\gamma/T} \ln \frac{0.2317 E_\gamma}{\alpha_s T}, \quad (28)$$

where $dR = dN/d^4x$. We use a temperature dependent running coupling constant

$$\alpha_s = \frac{6\pi}{(33 - 2n_f) \ln(T/\Lambda_T)}, \quad (29)$$

where we take $\Lambda_T = 40$ MeV [33] and, as in the EOS, $n_f = 2.5$.

For the hadron phase, we use the single photon production rates calculated in Ref. [50]. These calculations were performed using a pseudoscalar–vector Lagrangian of the form

$$\mathcal{L} = |D_\mu \Phi|^2 - m_\pi^2 |\Phi|^2 - \frac{1}{4} \rho_{\mu\nu} \rho^{\mu\nu} + \frac{1}{2} m_\rho^2 \rho_\mu \rho^\mu - \frac{1}{4} F_{\mu\nu} F^{\mu\nu}, \quad (30)$$

where Φ , A_μ and ρ_μ are complex pseudoscalar, photon and vector fields, respectively. Furthermore, $D_\mu = \partial_\mu - ieA_\mu - ig_\rho \rho_\mu$ is the covariant derivative, and $\rho_{\mu\nu}$ and $F_{\mu\nu}$ are the vector meson and electromagnetic field strength tensors, respectively. Also, $g_\rho^2/4\pi = 2.9$ as determined from the decay $\rho \rightarrow \pi\pi$.

Parameterizations of the rates contributing to $E_\gamma dR^{\text{HG}}/d^3p$ were given as a function of T and E_γ in Ref. [53] for the most important processes. These include the two scattering processes $\pi + \pi \rightarrow \rho + \gamma$ and $\pi + \rho \rightarrow \pi + \gamma$. The latter was only calculated for virtual pion exchange. It was shown in Ref. [54] that γ production in the π - ρ channel is dominated by the a_1 decays. Thus, we include the process $\pi + \rho \rightarrow a_1 \rightarrow \pi + \gamma$ by using the parametrization

given in Ref. [54]. The decays $\rho \rightarrow \pi\pi\gamma$ and $\omega \rightarrow \pi^0\gamma$, which occur during the lifetime of the fireball, were also included using the parametrization given in Ref. [53].

The total single photon spectrum is given by integrating over the total space-time volume, i.e., over all fluid cells with $\varepsilon \geq \varepsilon_f$:

$$E \frac{dN^\gamma}{d^3p} = \int d^4x \left\{ w(\varepsilon, \rho_B) E \frac{dR^{\text{QGP}}}{d^3p}(p \cdot u, T, \mu_B) + [1 - w(\varepsilon, \rho_B)] E \frac{dR^{\text{HG}}}{d^3p}(p \cdot u, T) \right\}, \quad (31)$$

where w is defined in Eq. (19). One should note that the rates are functions of $p \cdot u = p^\mu u_\mu$, the energy of the photons in the rest frame of the emitting fluid element. So far, the rates for the hadron phase do not contain processes involving baryons. Hence, there is no dependence on μ_B . Possible contributions from baryons to the thermal photon yields were estimated to be small, even for Pb + Pb collisions at the CERN-SPS in Ref. [55].

VII. DILEPTONS

We turn now to a discussion of dilepton production from both the quark-gluon plasma and the hadron gas. The dominant process in the QGP is the reaction $q\bar{q} \rightarrow l^+l^-$, which was computed in lowest order for finite baryon chemical potential to be [56]:

$$\frac{EdR^{\text{QGP}}}{dM^2 d^3p} = \frac{5}{9} \frac{\alpha^2}{8\pi^2} (1 + 2m_e^2/M^2) \sqrt{1 - 4m_e^2/M^2} e^{-E/T} \ln \frac{\{x_- + \exp[-(E + \mu)/T]\} [x_+ + \exp(-\mu/T)]}{\{x_+ + \exp[-(E + \mu)/T]\} [x_- + \exp(-\mu/T)]}, \quad (32)$$

where $x_\pm = \exp[-(E \pm |p|)/(2T)]$.

At low invariant masses, reactions at order $O(\alpha^2\alpha_s)$ become important [57]. However, the mass region where these corrections are significant is dominated by the Dalitz decays of the final mesons [58]. We have not taken these higher order contributions into account in our hydrodynamical simulations.

For the hadron gas contribution to the dilepton rate, we use the results of Ref. [59]. As in the calculation of the photon rates, the authors made use of the most general lowest order Lagrangian with vector and pseudoscalar mesons. The coupling of these fields to the electromagnetic current was computed under the assumption of Vector Meson Dominance. Prior to these calculations, the only rates computed were those due to $\pi\pi$ annihilation. The addition of other vector, pseudoscalar, and axial channels enhances the total rate by at least an order of magnitude away from the mass region of the light vector mesons. In doing so, however, one must not overcount channels already accounted for in the basic $\pi\pi$ reactions [60]. Therefore, the vector meson decays were excluded [61] from the total rate given in Ref. [59]. We have also verified that the rates used in our calculations are in essential agreement with those calculated recently in Ref. [62] using a spectral function approach.

We adopt the following procedure in incorporating these rates in our hydrodynamic simulations. Our starting point is the parametrization of the total dilepton production rate $dR^{\text{tot}}/dM^2(M, T)$ as a function of temperature T and invariant mass $M^2 = p^2 = (p_1 + p_2)^2$, as in Ref. [59]. Here, p , p_1 , and p_2 are the four-momenta of the pair and the single leptons, respectively.

In order to apply the kinematical cuts, we need the momentum distribution of the pair. To obtain this, we use the relation [63]

$$\frac{dR^{\text{HG}}}{dM^2 dy_T dp_T} = \frac{1}{2MTK_1(M/T)} e^{-E/T} \frac{dR^{\text{tot}}}{dM^2}(M, T), \quad (33)$$

where $E = p_\mu u^\mu$ is the pair energy and K_1 is a modified Bessel function. This relation is valid for reactions in which the final state contains only the lepton pair, which gives the dominant contribution in the higher mass region. However, the relation is not valid for the decays, $h \rightarrow h' e^+ e^-$, which result in small mass pairs. The region in which Eq. (33) is a good approximation was given to be above 300 MeV in invariant mass in [64]. We have verified that the approximation Eq. (33) adequately reproduces the rates in Ref. [62] above an invariant mass of 400 MeV. Below 400 MeV, differences may exceed a factor of 2 and

above in some regions of the phase space. However, in this region the spectrum is dominated by Dalitz decays of mesons *after freeze-out*, which are accurately treated separately.

The rates, Eq. (32) and Eq. (33), are integrated over the space-time volume of the fireball, as in Eq. (31) for the photons. Here also, we include baryon contributions from only the QGP phase. It remains to be seen whether baryons can contribute significantly to the dilepton yields (see for example, Ref. [65] for initial estimates).

The measured dilepton spectra also contain pairs from decays after freeze-out. We consider this as a background contribution. When comparing our results with the measurement of the CERES-collaboration [14], we calculate this background from our hydrodynamical simulation, instead of using the background estimated by the CERES-collaboration [14]. We combine the freeze-out momentum distributions of π^0 , η , ρ^0 , ω , η' , and ϕ as given by Eq. (27) with the distributions from the decays of higher lying resonances.

First, we consider the vector meson decays into electron pairs. The hydrodynamic calculation is done assuming a fixed mass and zero width for the resonance states. In order to calculate the dilepton spectra, we have to take into account at least the width of the ρ^0 meson. We assume that the mass distribution of the resonance is of the Breit-Wigner form:

$$\frac{EdN^V}{dM^2 d^3p} = \frac{\xi}{\pi} \frac{\Gamma_{\text{tot}}^2(M)}{(M^2 - m_V^2)^2 + \Gamma_{\text{tot}}^2(M)m_V^2} \frac{EdN^{\text{hydro}}}{d^3p}, \quad (34)$$

where m_V is the mean mass of the vector mesons. The normalization ξ is determined in such a way that the total yield has the value calculated at the freeze-out. We use the following mass dependence of the total ρ width [47]:

$$\Gamma_{\text{tot}}^\rho(M) = 3.15 \frac{(M^2 - 4m_\pi^2)^{3/2}}{1 + 39.7(M^2 - 4m_\pi^2)}. \quad (35)$$

with M and m_π in units of GeV. For the other vector mesons (ω , ϕ), constant widths taken from experiment [66] are used. This is justified, since the experimental resolution of CERES is much wider than these widths. In addition to the cuts $2m_\pi$ ($2m_K$) for ρ^0 (ϕ) at threshold,

we apply a cut $3m_\pi$ for the ω mass distribution. The electro-magnetic decay width in the Vector Meson Dominance model is proportional to the pair mass [56]. Hence, we use the parametrization

$$\Gamma_{V \rightarrow e^+e^-}(M) = \Gamma_{V \rightarrow e^+e^-}^{\text{exp}} \frac{M}{m_V}, \quad (36)$$

with the values of m_V and $\Gamma_{V \rightarrow e^+e^-}^{\text{exp}}$ taken from Ref. [66]. Thus, the electron pair distribution is given by

$$\frac{EdN^{\text{pair}}}{dM^2 d^3p} = \frac{\Gamma_{V \rightarrow e^+e^-}(M)}{\Gamma_{\text{tot}}^V(M)}(M) \frac{EdN^V}{dM^2 d^3p}. \quad (37)$$

Next, we consider the Dalitz-decays of the mesons. We use the differential decay width [67]

$$\begin{aligned} \frac{d\Gamma_{i \rightarrow j e^+ e^-}}{dM^2} &= \frac{\alpha \Gamma_{i \rightarrow j \gamma}}{3\pi M^2} (1 + 2m_e^2/M^2) \sqrt{1 - 4m_e^2/M^2} \\ &\times \left[\left(1 + \frac{M^2}{m_i^2 - m_j^2}\right)^2 - \frac{4m_i^2 M^2}{(m_i^2 - m_j^2)^2} \right] |F(M^2)|^2. \end{aligned} \quad (38)$$

If the particle j is a photon γ , the normalization to $\Gamma_{i \rightarrow \gamma \gamma}$ results in an additional factor of 2 on the r.h.s. of Eq. (38). For $\pi^0 \rightarrow \gamma e^+ e^-$, we take a linear approximation for the form factor, $F(M^2) = 1 + 5.5 \text{ GeV}^{-2} \times M^2$, from Ref. [67]. For $\eta \rightarrow \gamma e^+ e^-$ and $\omega \rightarrow \pi^0 e^+ e^-$, the dipole approximation, $F(M^2) = (1 - M^2/\Lambda^2)^{-1}$, with $\Lambda_\eta = 720 \text{ MeV}$ and $\Lambda_\omega = 650 \text{ MeV}$, respectively, is used. For $\eta' \rightarrow \gamma e^+ e^-$, the Vector Meson Dominance form factor

$$|F(M^2)|^2 = \frac{m_\rho^4}{(M^2 - m_\rho^2)^2 + m_\rho^2 \Gamma_{\text{tot}}^{\rho^2}}. \quad (39)$$

is used. The pair distribution is then calculated from

$$\frac{EdN^{\text{pair}}}{dM^2 d^3p} = \frac{1}{\Gamma_{\text{tot}}^{\text{exp}}} \frac{d\Gamma_{i \rightarrow j e^+ e^-}}{dM^2}(M) \frac{EdN^{i \rightarrow Mj}}{d^3p}(M), \quad (40)$$

where $\Gamma_{\text{tot}}^{\text{exp}}$ is taken from Ref. [66] and $EdN^{i \rightarrow Mj}/d^3p$ is an isotropic electron pair distribution resulting from the decay of an unpolarized meson i into a pair of mass M and a particle j , as given in Ref. [47]. The incorporation of the experimental cuts and resolution is described in the appendix.

VIII. RESULTS

In this section, we discuss the results of our attempt to describe consistently the hadron and electromagnetic spectra in S+Au collisions using the hydrodynamic approach. We fix the parameters for the initial conditions from the hadron spectra. In general, good fits are obtained only for the pion distributions — the fits to heavier hadron spectra are significantly worse. These are discussed in detail below. We apply the temperature and velocity distributions corresponding to these fits to predict the photon and dilepton spectra for each EOS. Our results may be summarized as follows. The existing photon data are not sufficiently precise to exclude any EOS except the EOS for an ideal, massless pion gas. Hopefully, future experiments will allow for better discrimination. With regard to the CERES dilepton data, none of the EOSs considered, in conjunction with the standard leading order dilepton rates, succeed in reproducing the observed excess of dileptons below the ρ peak.

A. Hadron Spectra

We begin our discussion with the results for the hadron spectra in S+Au collisions. In Fig. 4, we show the rapidity spectra for several hadrons obtained from calculations using three different EOSs. In choosing the parameters in the calculation, our main emphasis has been to reproduce the negative particle spectrum. In the case of the ideal pion gas EOS I, we assume that the negatives consist of negative massless pions only. For the EOSs A and B, both of which exhibit a phase transition, the initial conditions are quite similar, but for the two purely hadronic EOSs H and I, they differ considerably (c.f. Table II).

Let us first note the features that are common to the three different EOSs. For the negatively charged particles, which are mostly pions, the calculations are in good agreement with the data from NA35 [7]. This tells us that, by a suitable choice of the initial conditions, the flow of energy density across the freeze-out surface can be reproduced reasonably well

with all the EOSs considered. The three pion states carry roughly half of the total energy. The other half is carried mainly by the baryons.

The experimental net proton $p - \bar{p}$ distribution in Fig. 4 shows a large asymmetry with respect to the center of momentum. (The two data points with $y < 3$ are identified proton data from a different experiment NA44 [9] with S + Pb. It is instructive to view these points together with the net proton distribution from NA35 [6], because in this region the anti-proton yield is very small. While NA35 has practically a full p_T -acceptance up to 2 GeV, the NA44 data were extrapolated to the full p_T region.) There is a large difference in the target and projectile size, and we are presently unable to take this into account in our code with longitudinal mirror symmetry. However, we do not want to neglect the baryons totally, since they carry a significant part of the total energy; their influence is felt through the EOS during the space-time evolution. We reproduce the right total number of baryons in our calculation. Also, the baryon rapidity density in the central rapidity region ($y_{\text{cm}} = 2.6$) is roughly reproduced. This should ensure a reasonable description of the expansion in the central region, where our calculations of the electromagnetic yields are compared with measurements.

The K_s^0 distribution comes out too large in comparison with experiment. This may be attributed to the fact that we have assumed full chemical equilibrium. A detailed chemical analysis of strange particle spectra in the S + Au collisions in Ref. [32] shows a strangeness suppression of 0.7 relative to full chemical equilibrium. Multiplying the K_s^0 -spectra and the other strange particle spectra by this factor would improve the fit. The abundance of K_s^0 mesons is also slightly influenced by the baryon distributions through the requirement of strangeness neutrality. The K^+ and K^0 have to compensate the net negative strangeness of the Λ baryons. In the region $3 < y < 4$, the overestimation of the Λ 's leads to a small additional contribution to the K_s^0 's.

The Λ and $\bar{\Lambda}$ rapidity distributions are influenced both by the strangeness and the baryon

number chemical potentials. From the rapidity distribution of the protons, we see that the baryon number, or equivalently the baryon chemical potential, is too large in the forward rapidity region, because of the longitudinal symmetry in our calculation. The excess in the Λ spectrum in the region $3 < y < 4$ is similar to that for protons. In order to answer the question of how well strangeness chemical equilibrium holds for the strange baryons, we should first reduce μ_B to reproduce the proton distribution in this rapidity range. It seems that this would lead to a reasonable agreement for the Λ 's, assuming that μ_s would be unchanged. However, a reduction in μ_B would not be sufficient to increase the $\bar{\Lambda}$ yield to the experimental value at rapidities around 3.

We may summarize our analysis of the strange hadrons by stating that, for the freeze-out parameters that fit the negative particle yields, there is agreement in the yield of Λ 's relative to that of protons, but the $\bar{\Lambda}$'s are underestimated and the K_0 's are slightly overestimated. An analysis of S+S collisions at the same freeze-out temperature, $T_f = 140$ MeV, has led to the same conclusion [18,68].

The particle yields are determined in our model by the assumption of chemical equilibrium until freeze-out. This is poorly justified in the late dilute phase, since the strangeness changing cross sections are small. Therefore, a study of the chemical behavior in the late phase deserves further investigation on its own right, but is outside the scope of this investigation. However, looking at the pion distributions, we think that the bulk behavior of the longitudinal expansion is well reproduced by our model.

The transverse momentum distributions are shown in Fig. 5. The overall agreement is quite good with the exception of the EOS I. (We will return to discuss this case later.) The m_T -spectra of π^0 s are well fit up to 2 GeV. For larger transverse momenta, the three EOSs can also be distinguished. If one uses the same initial conditions, then a stiffer EOS would produce more transverse flow. However, to fit the longitudinal spectra, we enhanced the initial energy density for the EOS B and reduced it for the EOS H in comparison to that

for the EOS A (c.f. Table II). The initial temperatures are roughly the same in each case, and lead to the similar final p_T -slopes.

Although the best agreement is achieved using the EOS H, fits for the other EOSs can be improved by fine-tuning the initial conditions. Further, it is doubtful that particles with very large p_T follow a hydrodynamical behavior. Instead, they might originate from semi-hard processes. We therefore conclude that, with the exception of the EOS I, we cannot rule out any of the remaining three EOSs on the basis of fits to the p_T -spectra.

The ideal pion gas EOS I produces too flat a slope. The initial conditions in this case correspond to the same total energy as in the other three cases (see Table II). This was necessary in order to get the rapidity spectra correct in the central rapidity region. Since there are no baryons to share the energy, the surplus energy is converted to transverse kinetic energy. In short, for the EOS I, we could not find initial conditions which reproduce both the rapidity and p_T -spectra simultaneously (see also Ref. [70]). Therefore, the ideal pion gas EOS I can be ruled out, on the basis of hadronic data, as being too stiff.

The absolute yields of the other particles in Fig. 5 depend on the assumption of chemical equilibrium, the inadequacy of which we have discussed above. This is also corroborated by the the anti-proton yield, which is also underestimated, like that of the $\bar{\Lambda}$'s. We see, however, that the slopes for the different particles are reasonably reproduced by all three EOSs, supporting the picture of collective transverse flow present at SPS energies [17].

At low p_T , especially for the Λ 's, discrepancies between calculations and data persist. The calculation is expected to overshoot the data on the basis of the excess seen in the rapidity spectrum in the $3 < y < 4$ region. The larger relative weight from this region in the calculation as compared to the data might also be a reason for the difference in the slopes.

The experimental η/π^0 -ratio for central events [11] has large error bars. It is reproduced

reasonably well at large p_T , but our calculation underestimates it at low p_T . In our model, the 4π integrated η/π^0 -ratio depends mainly on the freeze-out temperature. In Table III, we compare the total multiplicities with $p + p$ data on meson production [69]. Our η/π^0 -ratio is similar to that in proton collisions and the minimum bias data in S + Au collisions [12].

To summarize the discussion of the hadron spectra, we see that with the exception of the ideal pion gas EOS, the initial conditions can be adjusted to reproduce the gross behavior of the hadron (negatives) spectra for a wide class of EOSs. Details of the spectra depend on the assumption of chemical equilibrium, which turns out to be poorly justified at freeze-out temperatures of $T_f \sim 140$ MeV. Chemical equilibrium between particles and resonances which have a large cross section may still hold.

B. Photon Spectra

The fundamental difference between the hadron spectra and the photon spectra is the fact that photons are emitted from collisions of charged particles during the entire expansion stage. We have calculated the photon p_T -spectra using *the same simulation* from which the hadron spectra were obtained. We integrate the photons over the four-dimensional space-time volume, Eq. (31), which is bounded by the three-dimensional freeze-out surface used for the calculation of the hadron spectra. The calculations are compared with the upper bound of the WA80 collaboration on the direct photon spectrum [13]. Experimentally, the direct photon yield is obtained by subtracting photons from the decays of mesons and baryons.

Since the photon yield depends on the properties of the system as it expands, we first discuss how the space-time behavior is affected by the different EOSs. In Fig. 6, contours of constant energy density in the zt -plane at $r = 0$ are shown, for all four EOSs. The boundaries of the mixed phase are indicated as solid lines. The freeze-out times at the center $z = 0$ are $t_f = 9.4, 7.9, 7.9,$ and 7.5 fm/ c for EOSs A, B, H, and I, respectively. At $r = 0$, transverse expansion is absent essentially up to t_f . Similar freeze-out times for

different EOSs indicate that the longitudinal expansion in the central region is dominated by the initial velocity gradient. At large z , the QGP equations of state produce a long-living tail. This is the result of a weaker longitudinal acceleration, due to the smaller pressure gradient in the mixed phase as compared with that in a calculation employing the hadron gas EOS without phase transition.

The space-time volume of the mixed phase in the EOS B is somewhat larger than that for the EOS A, despite the fact that it has a smaller latent heat, which allows, per unit volume, a faster conversion of the mixed phase into the hadron gas. However, for the EOS B, the mixed phase is reached at a later time and with so much larger volume that the conversion takes more time and produces a bigger final volume than that for the EOS A.

In Fig. 7a, we show the direct photon spectra for the EOS A. From the individual contributions from the different phases, it is clear that hadronic processes dominate the production of single photons in this case. In Ref. [50], it was shown that at the same temperature, emission rates per unit volume are roughly the same in a QGP and a hadron gas. Inclusion of the a_1 mesons enhances photon production for energies $E_\gamma > 1$ GeV [54], leading, at T_c , to a considerably larger photon production rate in the hadron gas than in the QGP. Also, the high temperature phase above T_c lasts for a short time in this case, and the produced matter spends most of its lifetime in the hadron gas phase. These two features lead to the dominance of photon emission from the hadronic phase. The higher temperature of the initial QGP phase shows up as a flatter p_T slope in the plasma contribution, but even at the largest p_T values, it is clearly below the hadron gas contribution. The total yield is in agreement with the upper bound provided by the data.

In Fig. 7b, the individual contributions are shown for the EOS B. In this case, the hadrons from the mixed phase dominate photon production. The QGP yields are similar to those with the EOS A. At large p_T , the QGP contribution is as large as the hadron contribution from the mixed phase. There is contribution from the pure hadron gas phase,

because the transition from the mixed phase to the hadron phase and freeze-out takes place simultaneously at the same temperature.

Figure 8 shows the total single photon spectra for the four different EOSs. The situation is qualitatively similar to that for the p_T -spectrum of π^0 's in Fig. 5. However, quantitative differences exist. A close inspection reveals that not only the results for the EOS I, but also for the other three EOSs, differ from one another. The total yield with the EOS B lies a factor 2–3 below that of the EOS A, whereas the EOS H produces 2–10 times more photons depending on the p_T -region. The yield for the EOS I lies orders of magnitude above.

In principle, the dependence of the photon production on T_c could be used to determine T_c from the data. However, one can see from Fig. 8 that the present upper bound on the single photon yield rules out only the ideal pion gas EOS I. (Recall that this EOS is also ruled out by the transverse momentum spectrum of negative hadrons.) From our results of the photon spectra, we cannot claim evidence for a phase transition, in contrast to the claims in Refs. [70–72]. The main point here is that, if a reasonable amount of degrees of freedom are taken into account in a hadron gas, the increase of temperature with energy density is reduced. This is clearly seen by comparing results for the EOS H with those for the EOS I. The large photon yield in the case of the EOS I is due to the very large initial temperature, $T_i = 400$ MeV, as compared to $T_i = 250$ MeV for the EOS H.

In the extreme case of the Hagedorn bootstrap model [31], we have a limiting temperature ~ 150 MeV in a hadron gas, with arbitrarily high energy densities. For limited energy densities, such an EOS would lead to a small photon production. Therefore, the results do not readily attest to the existence or the absence of a phase transition. With the present precision, one can only rule out high initial temperatures. However, since the rates from the hadron gas and the QGP differ, the correlation between the total yield and the slope of the transverse momentum distribution will differ for the purely hadronic EOS and an EOS with a phase transition. For this reason, improving the experimental upper limit and measuring

the yield of direct photons is very important.

In discussing the dependence of the photon production on the transition temperature T_c , one should keep in mind not only the limitations of hydrodynamics, but also the uncertainties in the rate calculations both in the QGP and a hadron gas near T_c . Our discussion above is based on the considerable difference in the rates at the same temperature between perturbative QCD results [52] and leading order estimates in a hadron gas [50,54].

1. Comparison with other works

Finally, we want to compare our results with other calculations of photon yields in the S + Au collisions, which have used hydrodynamics to describe the evolution of the produced matter. These earlier calculations were compared with the preliminary data of WA80 [10]. The new analysis by WA80 gives upper bounds, which are compatible with the preliminary data.

First, we confirm the result of Ref. [72] that the absolute normalization of the photon yield is sensitive to T_c and to the EOS. The calculation in Ref. [72] was done using a one-dimensional Bjorken-like hydrodynamical scenario, whereas we employ a three-dimensional expansion. The small differences in the photon yield from our results can be attributed to the differences in the hydrodynamical solutions. In Ref. [72], consistency with the preliminary data of WA80 was achieved with $T_c \approx 200$ MeV, while lower critical temperatures of around 150 MeV led to an underprediction of the preliminary WA80 data. Therefore, the possibility of a long-lived mixed phase, of duration 30-40 fm/ c , was suggested there. For the EOSs used in our three-dimensional calculations, T_c lies in the range 140-165 MeV and the duration of the mixed phase does not exceed 10 fm/ c . Since the present data provides an upper bound only, a long-lived scenario is not necessary with the lower values of T_c which we have been

using.

Our results roughly agree with the investigation in Ref. [73] as well. However, Arbex et al. [73] only investigated an EOS with T_c of 200 MeV. Since, as noted above, the absolute normalization of the photon spectra is sensitive to the critical temperature, their results agreed with the preliminary data of WA80.

In Refs. [70] and [71], an agreement with the preliminary data of WA80 was achieved using an EOS with T_c around 160 MeV, while our calculation with EOS A would underpredict this preliminary data by roughly a factor of 4. In Ref. [71], a rather low freeze-out temperature, $T_f = 100$ MeV, was chosen. We have checked that the photon yield increases by a factor of ~ 1.5 when the calculation is extended from a freeze-out temperature $T_f = 140$ MeV to $T_f = 100$ MeV. In Ref. [71], the neglect of baryons and the smaller number of mesons in the EOS leads to considerably longer lifetimes for the mixed and hadron phases. In addition, our three-dimensional calculations lead to more rapid cooling than that obtained using the scaling expansion, even when transverse expansion is included. A combination of these effects can explain the larger yield in Ref. [71].

C. Dielectrons

The other electromagnetic signal, measured in the S+Au collisions by the CERES collaboration [14], is the dielectron mass distribution. In these measurements, the dilepton background from the decays of final mesons is not subtracted, because the amounts of different mesons are not precisely known. Thus, we have two parts in the final dilepton yield. First, the emission during the lifetime of the fireball and, second, the electromagnetic decays of hadrons after the decoupling. The latter contribution is shown in Fig. 9 for the EOS A. This background is similar for the other EOSs, since the final hadron spectra are reproduced in each case by tuning the initial conditions, as discussed above. The calculation of the decay dilepton spectrum is described in Sec. VII and the appendix. All hadrons which produce

lepton pairs are considered. Both the thermal contribution and the contributions from the decays from heavier hadrons are included.

Our calculated background in Fig. 9 is basically in agreement with the estimated background in Ref. [14]. However, there are some differences in the total yields of the decaying mesons, since in our calculation the meson multiplicities are given by the calculated freeze-out conditions, mainly the assumed temperature, the effect of the baryon chemical potential being small. On the other hand, the CERES collaboration used the meson-to- π^0 ratios from p+p collisions [69] to fix the multiplicities of mesons from the measured π^0 spectrum [10]. In Table III, we present the meson yields normalized to the π^0 yield. Our η multiplicity is somewhat higher than in $p + p$ collisions, while that of the ρ^0 is slightly smaller. For the ω meson, the ratio is 3/4. The main differences in the input yields are those for the η' and ϕ . The contributions from the η' are negligible compared to those from the other dilepton sources. Thus, the only important difference with the CERES background is a factor of 4 in the ϕ -mass region; however, this is still in agreement with the data.

In Fig. 10a, we show the dileptons radiated during the lifetime of the fireball. These results are folded with the CERES cuts and the CERES resolution. Here, we see the same systematics as in the case of photons; the hadronic contribution dominates the yield. The largest contribution comes from the π - π annihilation to dielectrons via the ρ -form factor (Vector Dominance); this is seen as a peak at the ρ mass. As for the photons, the contribution from the pure hadron gas and the hadronic contribution in the mixed phase are equally important.

The sum of the background and the thermal emission is shown in Fig. 10b. We first note that thermal emission roughly fills the gap between the background and the data around and above the ρ mass, even though the calculated results tend to lie at the lower bound of the errors, especially for the EOS B. Note that the systematic and the statistical errors are

shown separately [74].

In the mass region between 200 and 600 MeV, our calculated results lie clearly below the data. While the calculation has a dip in this region between the contributions from the Dalitz pairs and the vector mesons, the data is flat and smooth. There have been several suggestions for the origin of the excess over the expected sources in this invariant mass region [65,75–78]. An interesting possibility for the explanation is a shift of the vector meson masses associated with the expected restoration of chiral symmetry as the transition temperature T_c is approached in the hadron gas. We have not tried to include this in our calculation. With an appropriate parametrization of the temperature and/or density dependence of the hadron masses, we most likely would be able to reproduce the data, but a consistent treatment in a hydrodynamical approach would require the incorporation of density dependent masses to also calculate the EOS and the decay rates. This is beyond the scope of the present work, and its proper implementation requires a major effort, which will be taken up separately.

Our conclusions for the EOS from the dilepton calculations are similar to those for photons. The absolute yields are sensitive to T_c , and the results for the EOS B with $T_c = 140$ MeV are below the data at all mass values. However, the differences are not as pronounced as for the photons, since the contributions from the decays of final hadrons have not been subtracted.

1. Comparison with other works

The excess production of low-mass dilepton pairs in S + Au collisions was recently addressed in Ref. [64] using a one-dimensional Bjorken-like expansion. In the invariant mass range $0.2 \text{ GeV} < M < 0.6 \text{ GeV}$, where the excess over expected sources is most evident, the data were underpredicted by about a factor of 4. Due to the high initial temperature ($T_i = 380 \text{ MeV}$) required to obtain similar results in a purely hadronic scenario, the case in which a QGP is admitted ($T_i = 198.7 \text{ MeV}$, $T_c = 160 \text{ MeV}$, $T_f = 140 \text{ MeV}$, and a mixed

phase duration $\sim 13 \text{ fm}/c$) was favored in this work.

Where the deviations from the data are largest, our three-dimensional calculations (with the same standard rates as above) underpredict the data by a much larger factor (of about 8-10). Several sources for the differences from Ref. [64] may be cited. These include the use of a more realistic EOS, a shorter duration of the mixed phase, and features specific to the three-dimensional flow of the matter emitting the lepton pairs. Clearly, a combination of these effects results in dilepton yields that are lower than in the case of a one-dimensional Bjorken evolution, even in the case where an EOS admitting a phase transition to the QGP is used. We also calculate the background contributions from the calculated hadron spectra, whereas the CERES background is used in Ref. [64].

A comparison of our hydrodynamical results with the alternative sequential scattering models (also termed as cascade or transport models) depends on the extent to which thermalization is achieved in the latter approach. Specific medium modifications of the vector meson properties, in particular a decrease in their masses, have been found to yield a satisfactory description of the CERES data [76,65]. Whether a similar approach can be satisfactorily adopted in hydrodynamical simulations is a challenging future task.

IX. CONCLUSION

The aim of this work was to establish the extent to which one can constrain the EOS from the experimental data for S + Au collisions from a simultaneous description of the hadron and electromagnetic spectra using hydrodynamics. We have shown that, in general, the influence of the EOS on hadronic spectra can be counterbalanced by choosing different initial conditions. A simultaneous calculation of the electromagnetic signals can, in principle, distinguish between the different EOSs. However, the present experimental resolution allows us to rule out only extreme cases, such as the ideal pion gas EOS with only a few degrees of freedom. Also, the dilepton yield for the QGP equation of state with $T_c \simeq 140 \text{ MeV}$, the EOS B, tends to fall below the data in the vector meson mass region, indicating an effective

lower bound of 140 MeV for T_c , if the transition exists.

The constraint that can be drawn from the single photon data is that the initial temperature cannot be too high. The present data rules out temperatures above 250 MeV. This limit on the initial temperature can be achieved only if a large number of degrees of freedom is involved, be it in the form of quarks and gluons, or in the form of a large enough number of hadrons. However, if the data can be improved, the two cases can be distinguished, since the total emission from a hadron gas is larger than that from the QGP. In the total yield, the difference between a pure hadronic EOS and an EOS with a phase transition increases with decreasing T_c .

The behavior of the dilepton spectrum in the mass region between 200 and 600 MeV shows that the description of the hot and dense strongly interacting matter near T_c in terms of the free-space parameters is not adequate. With our present hydrodynamical approach, the dilepton spectrum can be explained only in the mass region of the vector mesons. The large experimental dilepton yield below the ρ mass may indicate medium modifications of the particle properties. These effects can be included in hydrodynamical calculations, but for a consistent calculation, the EOS must be modified accordingly.

ACKNOWLEDGMENT

We gratefully acknowledge helpful discussions with G.E. Brown, C. Gale, P. Lichard, H. Sorge, J. Steele, and I. Zahed. We thank E.K. Popenoe for a careful reading of the paper. J.S. acknowledges the kind hospitality of the INT in Seattle and the Department of Physics at SUNY in Stony Brook, where part of this work was done. P.H.'s work is supported by a grant from the Academy of Finland. The research of M.P. is supported by the U.S. Department of Energy under Grant number DE-FG02-88ER-40388. R.V.'s research at the INT is supported by DOE Grant DE-FG06-90ER40561.

APPENDIX

CUTS AND RESOLUTION FOR COMPARISON WITH CERES

The kinematic cuts of the CERES experiment are cuts in the momenta of the electron and the positron [14]. We incorporate them in the following way. We take $dN/(dM^2 dy p_T dp_T)$ of the pair calculated either from the background contribution (see Eq. 37 and Eq. 40) or that resulting from the fireball during its lifetime (see Eq. (32) and Eq. (33)). Going to the pair rest frame, we assume an isotropic momentum distribution. Thus, the single electron momentum distribution $dN/(dM^2 dy_1 p_{1T} dp_{1T})$, when the pair mass is M , is given by

$$\begin{aligned} \frac{dN}{dM^2 dy_1 p_{1T} dp_{1T}} &= \frac{M}{2\pi \sqrt{(M^2 - 4m_e^2)}} \int_{y^-}^{y^+} dy \int_{(m_T^-)^2}^{(m_T^+)^2} dm_T^2 \theta(p_{2T} - p_T^{\text{cut}}) \\ &\times \theta(\eta_{\text{max}}^{\text{cut}} - y_2 - y_{\text{cm}}) \theta(y_2 + y_{\text{cm}} - \eta_{\text{min}}^{\text{cut}}) \theta(\vartheta_{12}^{\text{lab}} - \Theta^{\text{cut}}) \\ &\times \frac{1}{\sqrt{p_T^2 p_{1T}^2 - [M^2/2 - m_T m_{1T} \cosh(y_1 - y)]^2}} \frac{dN}{dM^2 dy p_T dp_T}, \end{aligned} \quad (41)$$

where y , y_i are the rapidities in the fireball rest frame. Further,

$$\begin{aligned} y^\pm &= y_1 \pm \sinh^{-1}[\sqrt{(M^2 - 4m_e^2)}/(2m_{1T})] \\ m_T^\pm &= \frac{M}{2} \frac{M m_{1T} \cosh(y - y_1) \pm p_{1T} \sqrt{M^2 - 4m_e^2 - 4m_{1T}^2 \sinh^2(y - y_1)}}{m_{1T}^2 \sinh^2(y - y_1) + m_e^2}. \end{aligned} \quad (42)$$

The opening angle of the electrons in the laboratory system, $\vartheta_{12}^{\text{lab}}$, neglecting the electron mass, is given by

$$\cos(\vartheta_{12}^{\text{lab}}) = 1 - \frac{M^2}{2|p_1|^{\text{lab}}|p_2|^{\text{lab}}} \quad (43)$$

with $|p_i|^{\text{lab}} = p_{iT} \sqrt{1 + \sinh^2(y_i + y_{\text{cm}})}$.

The final spectrum of the pairs in the approximation $\eta_{e^\pm} = y_{e^\pm}$ is then

$$\frac{dN^{\text{cut}}}{dM d\eta} = \frac{2M}{\Delta \eta^{\text{exp}}} \int_{p_T^{\text{cut}}} dp_{1T} p_{1T} \int_{\eta^{\text{cut}}} dy_1 \frac{dN}{dM^2 dy_1 p_{1T} dp_{1T}}. \quad (44)$$

In order to compare with the CERES experiment, we finally have to fold the calculated results with the detector resolution. We use a Gaussian folding

$$\frac{dN^{\text{CERES}}}{dM d\eta}(M) = \int dM' \frac{1}{\sqrt{2\pi}\sigma(M')} \exp\left(-\frac{(M - M')^2}{2\sigma^2(M')}\right) \frac{dN^{\text{cut}}}{dM d\eta}(M'), \quad (45)$$

with the width $\sigma(M)$ taken to be the detector resolution kindly provided to us by the CERES collaboration [74].

REFERENCES

- [1] L.D. Landau, *Izv. Akad. Nauk. SSSR* **17** (1953) 51.
- [2] For reviews see:
H. Stöcker and W. Greiner, *Phys. Rep.* **137**, (1986) 277;
J.P. Blaizot and J.Y. Ollitrault, in [4], p. 393.
- [3] R.B. Clare and D. Strottman, *Phys. Rep.* **141**, (1986) 177.
- [4] See for example, *Quark-Gluon Plasma* and *Quark-Gluon Plasma 2*, R.C. Hwa (ed.),
World Scientific, Singapore, 1990, 1995, respectively.
- [5] T. Alber et al. (NA35 collaboration), *Z. Phys.* **C64**, (1994) 195.
- [6] D. Röhrich et al. (NA35 collaboration), *Nucl. Phys.* **A566**, (1994) 35c.
- [7] M. Gaździcki et al. (NA35 collaboration), *Nucl. Phys.* **A590**, (1995) 197c.
- [8] J. Günther et al. (NA35 collaboration), *Nucl. Phys.* **A590**, (1995) 487c.
- [9] M. Murray et al. (NA44 collaboration), AIP Conference Proceedings **340**, *Strangeness '95*, J. Rafelski (eds.), AIP Press, 1995, p. 162.
- [10] R. Santo et al. (WA80 collaboration), *Nucl. Phys.* **A566**, (1994) 61c.
- [11] A. Lebedev et al. (WA80 collaboration), *Nucl. Phys.* **A566**, (1994) 355c.
- [12] R. Albrecht et al. (WA80 collaboration), *Phys. Lett.* **B361**, (1995) 14.
- [13] R. Albrecht et al. (WA80 collaboration), *Phys. Rev. Lett.* **76**, (1996) 3506
- [14] G. Agakichiev et al. (CERES collaboration), *Phys. Rev. Lett.* **75**, (1995) 1272.
- [15] R. Venugopalan, M. Prakash, M. Kataja, and P.V. Ruuskanen, *Nucl. Phys.* **A566**,
(1994) 473c.
- [16] U. Ornik, F.W. Pottag, and R.M. Weiner, *Phys. Rev. Lett.* **63**, (1989) 2641.

- [17] E. Schnedermann and U. Heinz, *Phys. Rev. Lett.* **69**, (1992) 2908;
 E. Schnedermann, J. Sollfrank, and U. Heinz, *Phys. Rev.* **C48**, (1994) 2468.
- [18] J. Bolz, U. Ornik, and R.M. Weiner, *Phys. Rev.* **C46**, (1992) 2047.
- [19] U. Katscher et al. , *Z. Phys.* **A346**, (1993) 209.
- [20] H. von Gersdorff, L. McLerran, M. Kataja, and P.V. Ruuskanen, *Phys. Rev.* **D34**,
 (1986) 794.
- [21] J.P. Boris and D.L. Book, *J. Comp. Phys.* **A11**, (1973) 38;
 D.L. Book, J.P. Boris and K. Hain, *J. Comp. Phys.* **A18**, (1975) 248.
- [22] M. Kataja, *Z. Phys.* **C38**, (1988) 419.
- [23] S.T. Zalesak, *J. Comp. Phys.* **A31**, (1979) 335.
- [24] D.H. Rischke, S. Bernard, and J.A. Mahrun, *Nucl. Phys.* **A595**, (1995) 346.
- [25] F. Karsch, *Nucl. Phys.* **A590** (1995) 367c.
- [26] T. Blum, S. Gottlieb, L. Kärkkäinen, and D. Toussaint, *Nucl. Phys.* **B** (Proc. Suppl.)
42 (1995) 460.
- [27] J.-P. Blaizot and J. Y. Ollitrault, *Nucl.Phys.* **A458** (1986) 745; D.H. Rischke and M.
 Gyulassy, *Nucl.Phys.* **A597** (1996) 701.
- [28] R. Venugopalan, Ph. D. Thesis, SUNY Stony Brook, August 1992, Unpublished.
- [29] G. Welke, R. Venugopalan and M. Prakash, *Phys. Lett.* **245** (1990) 137.
- [30] R. Venugopalan and M. Prakash, *Nucl. Phys.* **A546**, (1992) 718.
- [31] R. Hagedorn and J. Ranft, *Nuovo Cim. Suppl.* **6** (1968) 169;
 R. Hagedorn, in *Hot Hadronic Matter: Theory and Experiment*, J. Letessier et al. (Eds.),
 Plenum, New York, 1995, and references therein.

- [32] J. Letessier, A. Tounsi, U. Heinz, J. Sollfrank, and J. Rafelski, *Phys. Rev.* **D51**, (1995) 3408.
- [33] J. Kapusta, “Finite Temperature Field Theory”, Cambridge University Press, Cambridge, 1989.
- [34] J.I. Kapusta and K.A. Olive, *Nucl. Phys.* **A408**, (1983) 478.
- [35] J.D. Walecka, *Ann. Phys.(NY)* **83**, (1974) 491; B.D Serot and J.D. Walecka, *Advances in Nuclear Physics*, Vol 16, ed. J.W. Negele and E. Vogt (Plenum, NY, 1986); B.D. Serot, *Rep. Prog. Phys.* **55** (1992) 1855.
- [36] W. Greiner, “Thermodynamics and Statistical Mechanics”, Springer Verlag, New York, 1995.
- [37] D.H. Rischke, Y. Pürsün, and J.A. Mahrun, *Nucl. Phys.* **A595**, (1995) 383.
- [38] J.D. Bjorken, *Phys. Rev.* **D27**, (1983) 140.
- [39] V. Blobel et al., *Nucl. Phys.* **B69**, (1974) 454.
- [40] I. Otterlund, *Nucl. Phys.* **A418**, (1983) 98c.
- [41] R.D. Woods and D.S. Saxon, *Phys. Rev.* **95**, (1954) 577.
- [42] J.L. Goity and H. Leutwyler, *Phys. Lett.* **B228**, (1989) 517.
- [43] M. Prakash, M. Prakash, R. Venugopalan and G. Welke, *Phys. Rep.* **227**, (1993) 323; *Phys. Rev. Lett.* **70**, (1993) 1228.
- [44] E. Schnedermann and U. Heinz, *Phys. Rev.* **C50**, (1994) 1675.
- [45] H. Sorge, *Phys. Lett.* **B373**, (1996) 16
- [46] F. Cooper and G. Frye, *Phys. Rev.* **D10**, (1974) 186.
- [47] J. Sollfrank, P. Koch, and U. Heinz, *Z. Phys.* **C52**, (1991) 593.

- [48] C. Gale and J. Kapusta, *Nucl. Phys.* **B357**, (1991) 65.
- [49] E. Braaten and R.D. Pisarski, *Nucl. Phys.* **B337**, (1990) 569.
- [50] J. Kapusta, P. Lichard, and D. Seibert, *Phys. Rev.* **C45**, (1991) 2774.
- [51] R. Baier, H. Nakkagawa, A. Niégawa, and K. Redlich, *Z. Phys.* **C53**, (1992) 433.
- [52] C. Traxler, H. Vija, and M. Thoma, *Phys. Lett.* **B346**, (1995) 329.
- [53] H. Nadeau, J. Kapusta, and P. Lichard, *Phys. Rev.* **C45**, (1992) 3034; *Phys. Rev.* **C47**, (1993) 2426.
- [54] L. Xiong, E. Shuryak, and G.E. Brown, *Phys. Rev.* **D46**, (1992) 3798.
- [55] P. Lichard and M. Prakash, to be published.
- [56] J. Cleymans, J. Fingberg, and K. Redlich, *Phys. Rev.* **D35**, (1987) 2153.
- [57] E. Braaten, R.D. Pisarski and T.-C. Yuan, *Phys. Rev. Lett.* **64**, (1990) 2242.
- [58] T. Altherr and P.V. Ruuskanen, *Nucl. Phys.* **B380**, (1992) 377.
- [59] C. Gale and P. Lichard, *Phys. Rev.* **D49**, (1994) 3338.
- [60] P. Lichard, *Phys. Rev.* **D49**, (1994) 5812.
- [61] P. Lichard, private communication.
- [62] J. Steele, H. Yamagishi, and I. Zahed , *Phys. Lett.* **B** , (1996) to be published.
- [63] D.K. Srivastava, J. Pan, V. Emel'yanov, and C. Gale, *Phys. Lett.* **B329**, (1994) 157.
- [64] D.K. Srivastava, B. Sinha, and C. Gale, *Phys. Rev.* **C53**, (1996) R567.
- [65] W. Cassing, W. Ehehalt, and C.M. Ko, *Phys. Lett.* **B363**, (1995) 35.
- [66] Particle Data Group, *Phys. Rev.* **D50**, (1994) 1173.
- [67] L.G. Landsberg, *Phys. Rep.* **128**, (1985) 301.

- [68] P. Huovinen, M.Sc. thesis, University of Jyväskylä, 1996, unpublished.
- [69] M. Aguilar–Benitez et al. (NA27 collaboration), *Z. Phys.* **C50**, (1991) 405.
- [70] A. Dumitru et al., *Z. Phys.* **C51**, (1995) 2166.
- [71] D.K. Srivastava and B. Sinha, *Phys. Rev. Lett.* **73**, (1994) 2421;
D.K. Srivastava and B. Sinha, *Nucl. Phys.* **A590**, (1995) 507c.
- [72] E.V. Shuryak and L. Xiong, *Phys. Lett.* **B333**, (1994) 316.
- [73] N. Arbex, U. Ornik, M. Plümer, A. Timmermann, and R.M. Weiner, *Phys. Lett.* **B354**, (1995) 307.
- [74] I. Tserruya, private communication.
- [75] P. Koch, *Z. Phys.* **C57**, (1993) 283.
- [76] G.Q. Li, C.M. Ko, and G.E. Brown, *Phys. Rev. Lett.* **75**, (1995) 4007; G.Q. Li, C.M. Ko, and G.E. Brown, *Nucl. Phys.* **A**, (1996) , to be published.
- [77] J. Kapusta, D. Kharzeev, and L. McLerran, *Phys. Rev.* **D53**, (1996) 5028
- [78] K. Redlich, J. Cleymans, and V.V. Goloviznin, University of Bielefeld preprint, BI–TP–94–48.

TABLE I. Some physical features characterizing various model EOSs.

	EOS A	EOS B	EOS H	EOS I
Hadronic	$\pi, K, \eta, \rho, \omega, K^*$	$\pi, K, \eta, \rho, \omega, K^*$	$\pi, K, \eta, \rho, \omega, K^*$	
Degrees of freedom	$p, n, \eta', \phi, \Lambda, \Sigma$	$p, n, \eta', \phi, \Lambda, \Sigma$	$p, n, \eta', \phi, \Lambda, \Sigma$	
	$\Delta, a_1, \Xi, \Sigma(1385)$	$\Delta, a_1, \Xi, \Sigma(1385)$	$\Delta, a_1, \Xi, \Sigma(1385)$	π
Number of QGP degrees of freedom	31	31	—	—
Mean field repulsion K [fm ³ MeV]	450	660	450	0
Bag constant $B^{1/4}$ [MeV]	235	200	—	—
T_c [MeV]	165	140	∞	∞
μ_{Bc} [MeV]	1770	1290	∞	∞
$\Delta\varepsilon$ [GeV/fm ³]	1.4	0.8	0	0

TABLE II. Variables used for the parametrization of the initial and freeze-out conditions for the different EOSs. The first part contains the free parameters, the second part some deduced quantities, and the third part the freeze-out energy density, with the corresponding temperature and baryon chemical potential averaged over the freeze-out hypersurface. The symbols are explained in the text.

	EOS A	EOS B	EOS H	EOS I
r_0 [fm]	3.65	3.65	3.65	3.65
a_r [fm]	0.50	0.50	0.50	0.50
z_0 [fm]	0.80	0.80	1.2	1.97
a_z [fm]	0.13	0.13	0.13	0.13
ε_0 [GeV/fm ³]	7.0	8.0	5.0	3.3
b_0 [fm ⁻³]	1.10	1.16	0.75	0
t_0^{-1} [c/fm]	1.06	0.95	0.71	0.41
$y(z = z_0)$	0.85	0.76	0.85	0.80
E_{tot} [GeV]	914	923	904	994
B_{tot}	105	104	104	0
S_{tot}	3880	4230	3650	3035
S/B	37	41	35	–
$T_i(z = 0)$ [MeV]	238	249	248	400
t_f [fm/c]	9.4	7.9	7.9	7.5
ε_{dec} [GeV/fm ³]	0.165	0.15	0.165	0.05
$\langle T_f \rangle$ [MeV]	142	141	142	140
$\langle \mu_{Bf} \rangle$ [MeV]	230	210	235	0

TABLE III. Total multiplicities used to estimate the background to the dielectron spectrum. The total yields are normalized to the π^0 yield. The EOS A is used in the calculation. For comparison, the total production cross section in $p + p$ collisions at 400 GeV incident momentum are shown in the first column (the data are taken from NA27 [69]).

	Hydro		NA27	
	total multiplicity	relative to π^0	total cross section [mb]	relative to π^0
π^0	212	1.000	127.2	1.000
η	19.4	0.092	9.8	0.077
ρ^0	18.6	0.088	12.6	0.099
ω	15.8	0.074	12.8	0.101
η'	2.0	0.009	–	–
ϕ	4.1	0.019	0.62	0.005

FIGURE CAPTIONS

Fig. 1. Phase diagrams for two equations of state with a first order phase transition. The meaning of the parameters is explained in the text. For the EOS A, $K = 450 \text{ MeV fm}^3$, $B^{1/4} = 235 \text{ MeV}$, and for the EOS B, $K = 660 \text{ MeV fm}^3$, $B^{1/4} = 200 \text{ MeV}$.

Fig. 2. Pressure P as a function of baryon ρ_B and energy densities ε for the EOS A (a) and the EOS B (b).

Fig. 3.

Initial conditions for S + Au collisions at $200 A \text{ GeV}/c$ for the case of the EOS A. The different panels show (a) the rapidity y , (b) the longitudinal velocity v_z , (c) the energy density ε , and (d) the baryon density ρ_B as a function of the longitudinal coordinate z ; (e) the baryon density ρ_B as a function of rapidity y ; (f) the energy density ε as a function of radius r .

Fig. 4. Rapidity distributions for several hadrons compared with a symmetric hydrodynamical calculation. The equations of state are EOS A (solid line), EOS B (dotted line), hadronic EOS H (short dashed line), and ideal pion gas EOS I (long dashed line). The data are measured by the following groups: Negative charged particle data are from NA35 [7], the strange hadron (Λ , $\bar{\Lambda}$, K_s^0) data from NA35 [5], the net proton ($p - \bar{p}$) data, with $y > 3$ from NA35 [6], and the two points of proton data with $y < 3$ are from NA44 [9].

Fig. 5. Transverse momentum distributions for several hadrons compared with a symmetric hydrodynamical calculation. Curve designations are as in Fig. 4. The data are measured by the following groups: π^0 data for central S + Au collisions from WA80 [10], the strange hadron (Λ , $\bar{\Lambda}$, K_s^0) data [5], and the anti-protons are from NA35 [8], and the η/π^0 ratio for central S + Au collisions from WA80 [11].

Fig. 6. Contours of constant energy density in the zt -plane for calculations with the EOS

A (a), EOS B (b), EOS H (c), and EOS I (d). Contours counted outward correspond to energy densities of 4.0, 2.0, 0.9, 0.4, 0.15 GeV/fm³ for (a) through (c), and to 2.0, 0.9, 0.4, 0.15, 0.05 GeV/fm³ for (d). The solid lines indicate the transition from the QGP to the mixed phase and from the mixed phase to the hadronic phase. The dashed line corresponds to freeze-out. In (b), freeze-out occurs at the transition from the mixed to the hadronic phase. Note the different scale in (b).

Fig. 7. Single photon p_T -spectra compared with the upper bound of WA80 data [13]; (a) EOS A and (b) EOS B. The different contributions shown are: HG hadron gas, M(HG) hadronic part of the mixed phase, M(QGP) QGP part of the mixed phase, QGP, and the total spectrum (solid line).

Fig. 8. Total spectrum of single photons for the different EOSs. The data are as in Fig. 7.

Fig. 9. Estimate of the background to the dielectron spectrum from the meson decays after freeze-out as calculated from the hydrodynamical result for the EOS A. The kinematic cuts and the detector resolution of the CERES experiment [14] are incorporated.

Fig. 10. Dielectron spectra compared with the measurement of the CERES collaboration [14]. Kinematic cuts and detector resolution are incorporated. (a) Contributions during the lifetime of the fireball. (b) Total dielectron spectrum including our background estimate for the different equations of state.

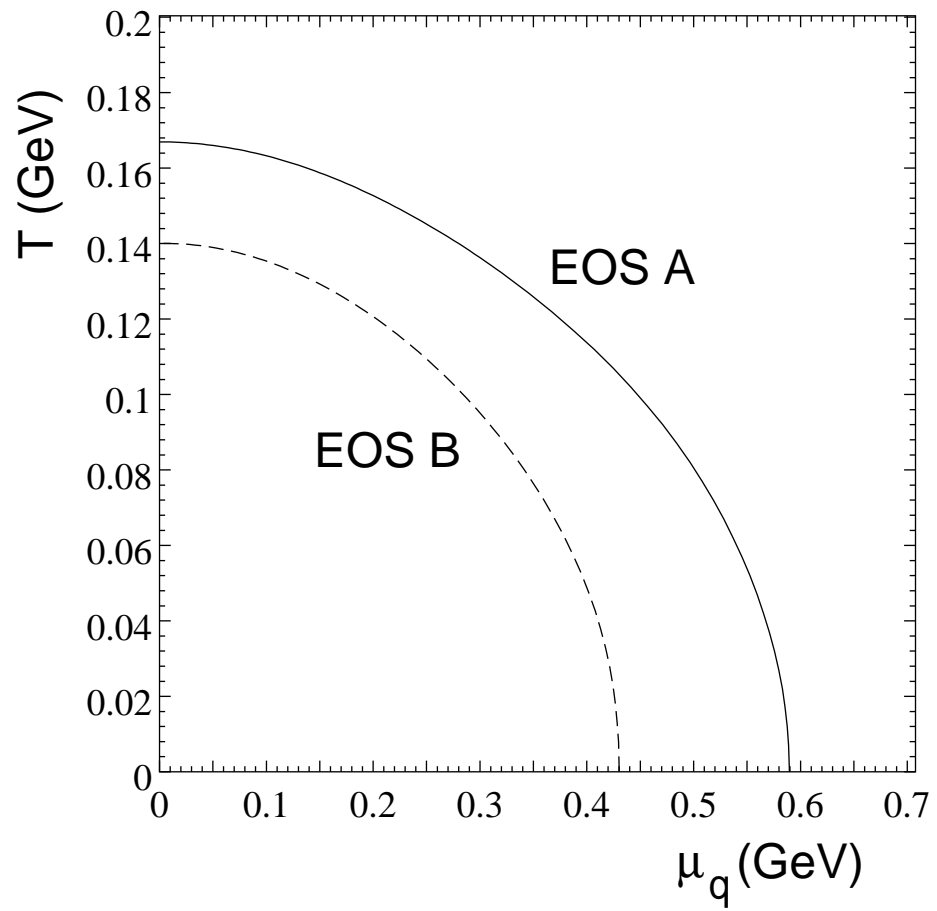


Figure 1

(a)

EOS A

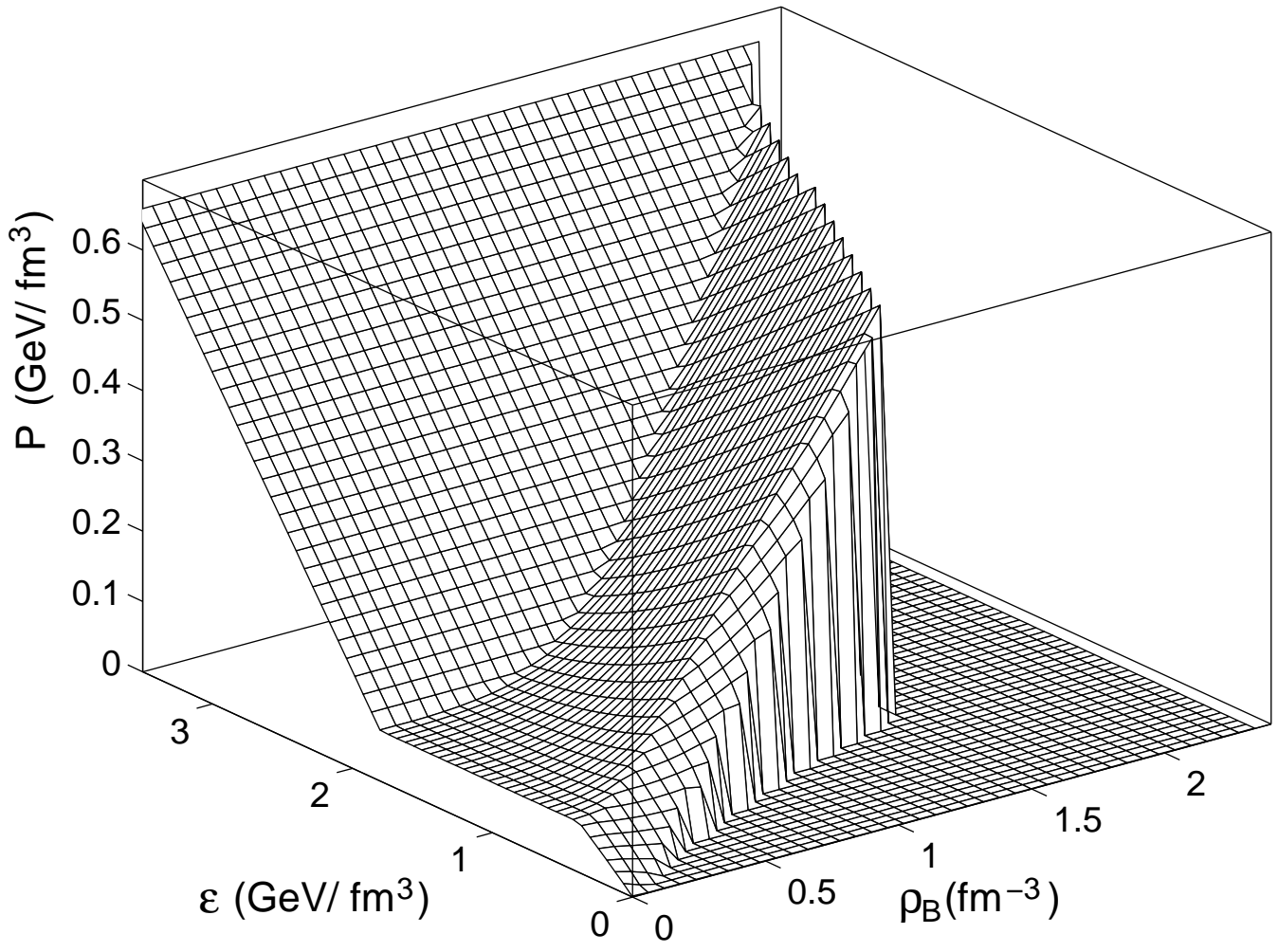


Figure 2 a

(b)

EOS B

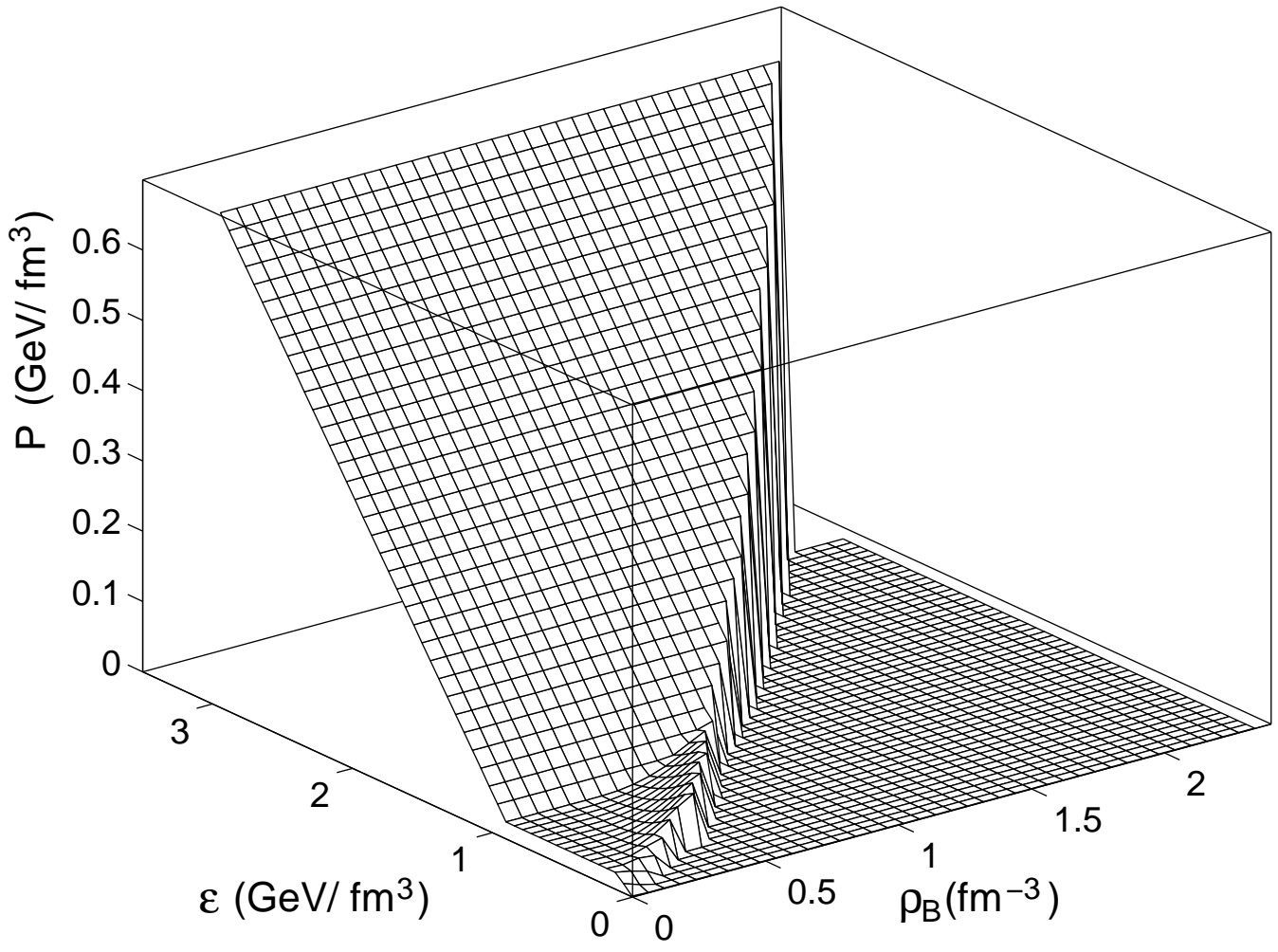


Figure 2 b

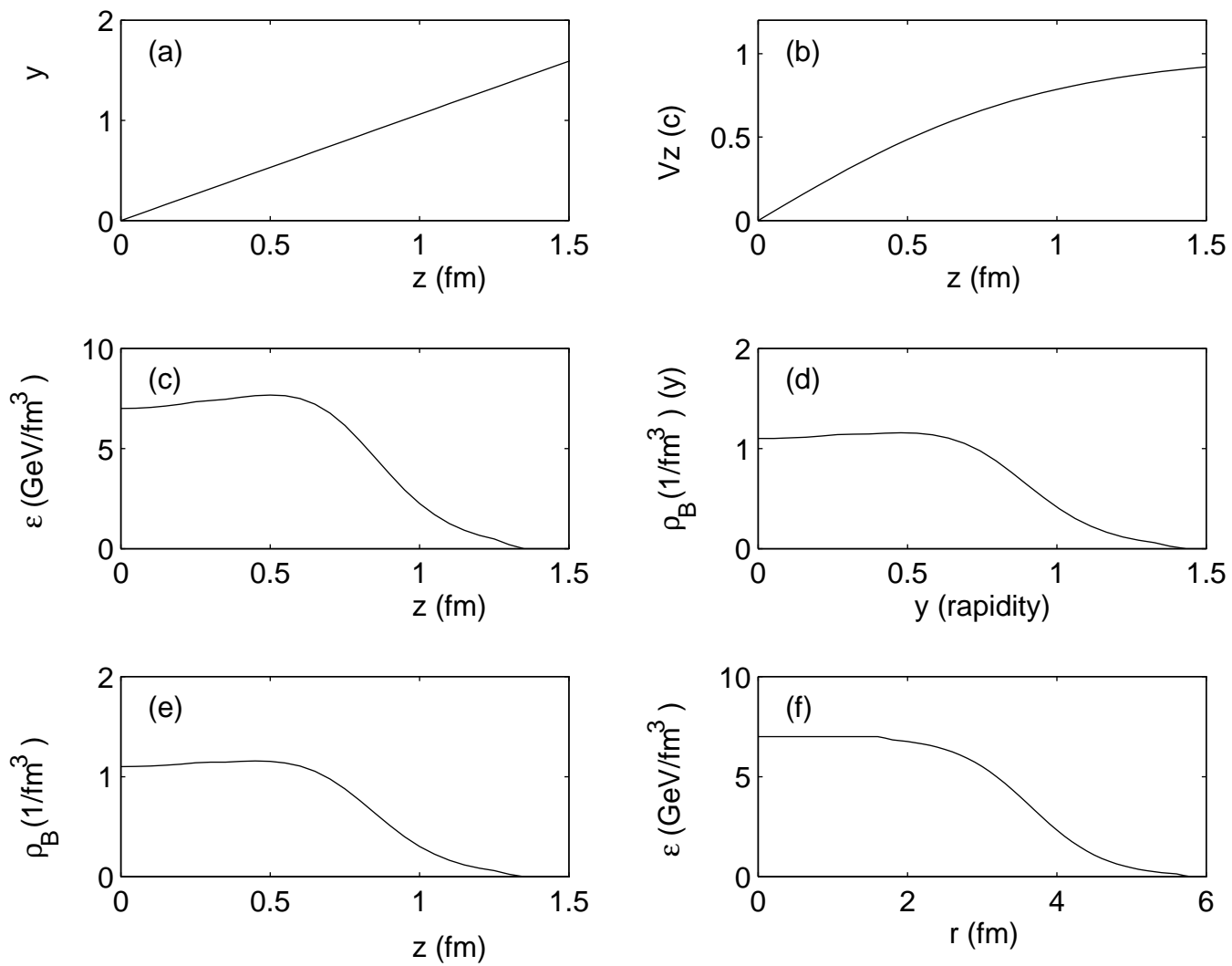


Figure 3

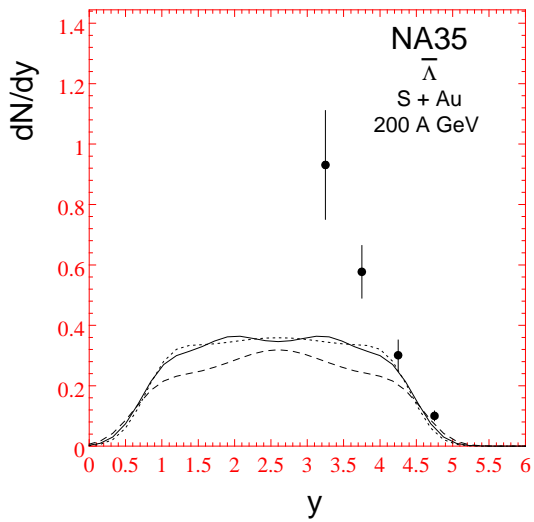
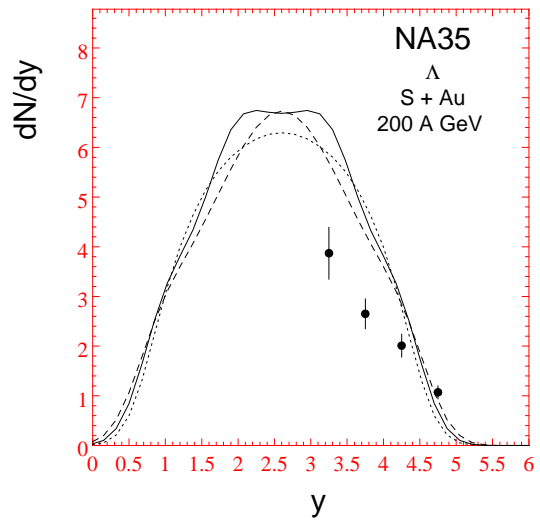
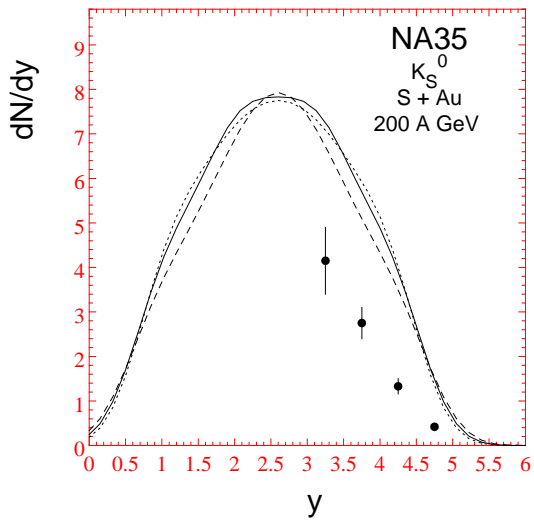
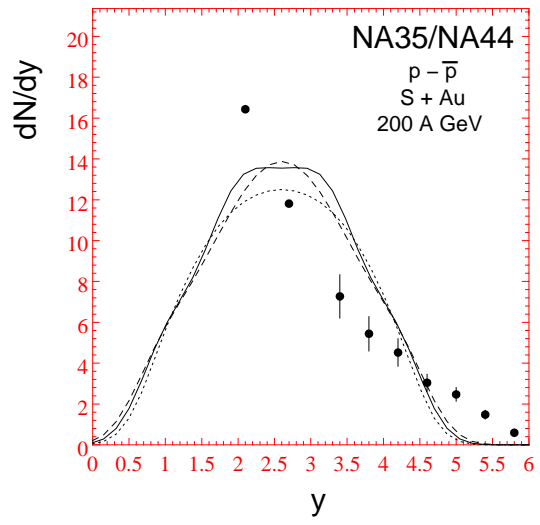
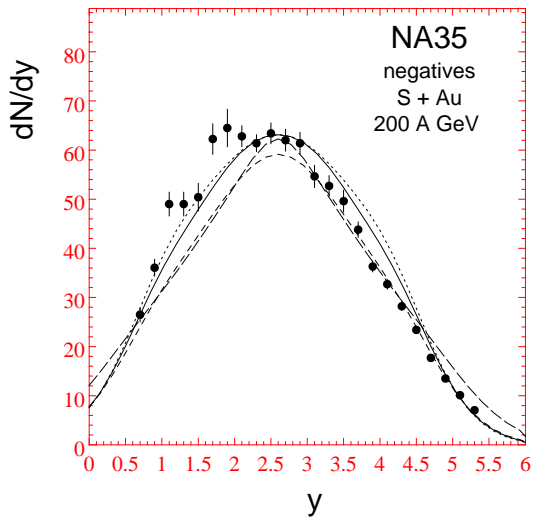


Figure 4

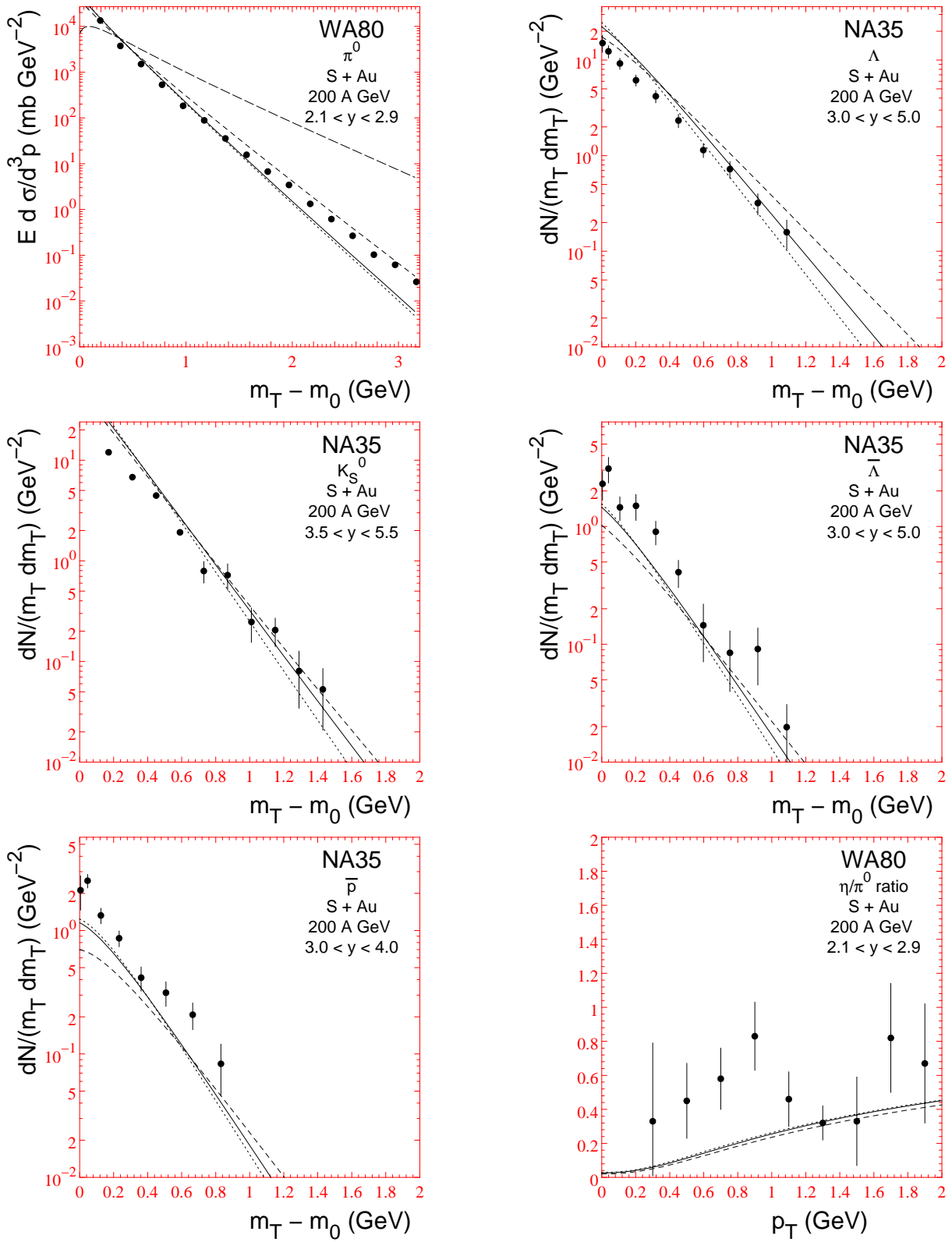


Figure 5

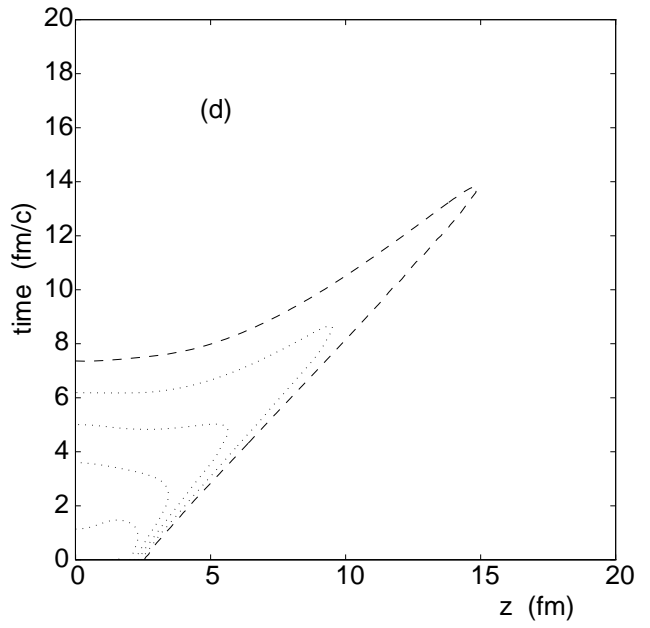
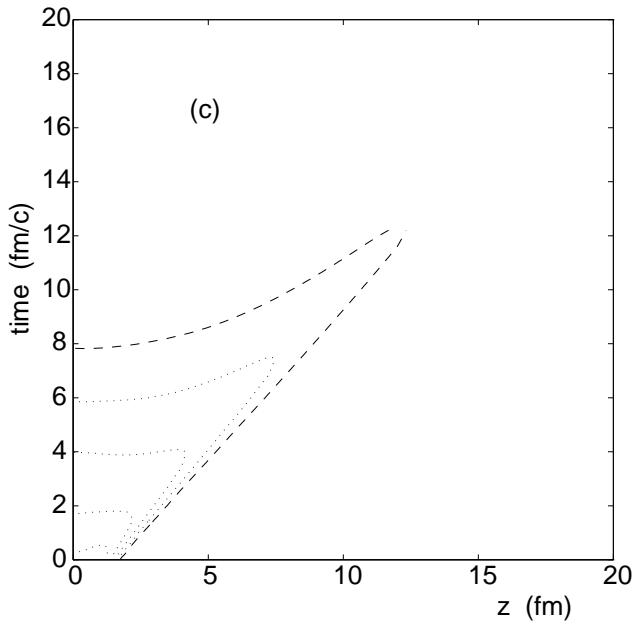
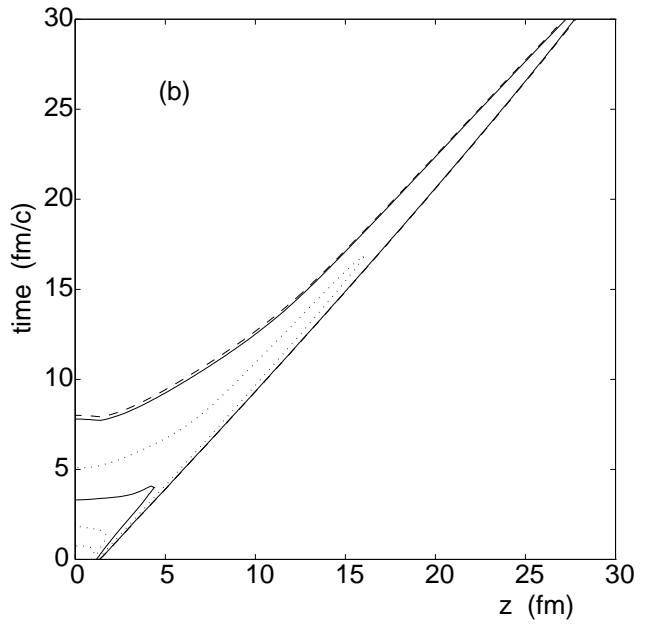
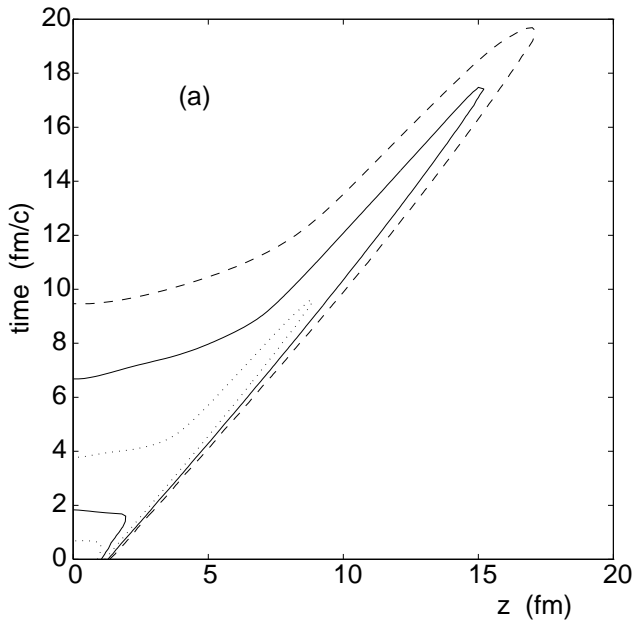


Figure 6

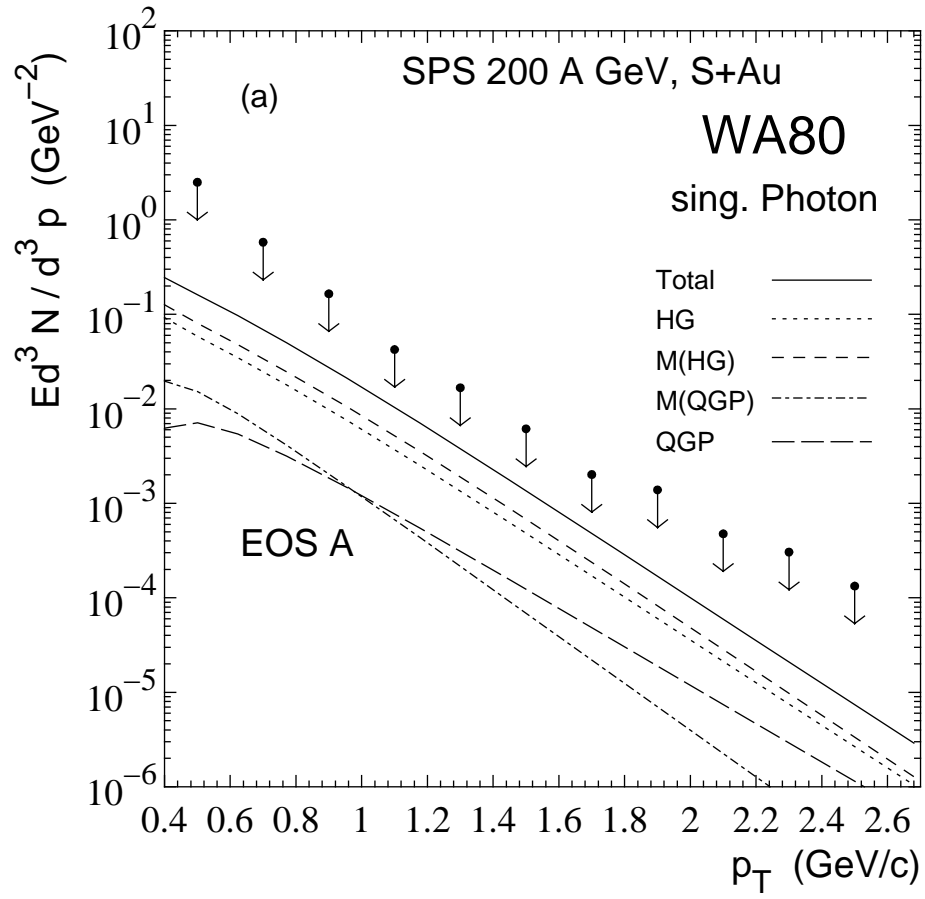


Figure 7a

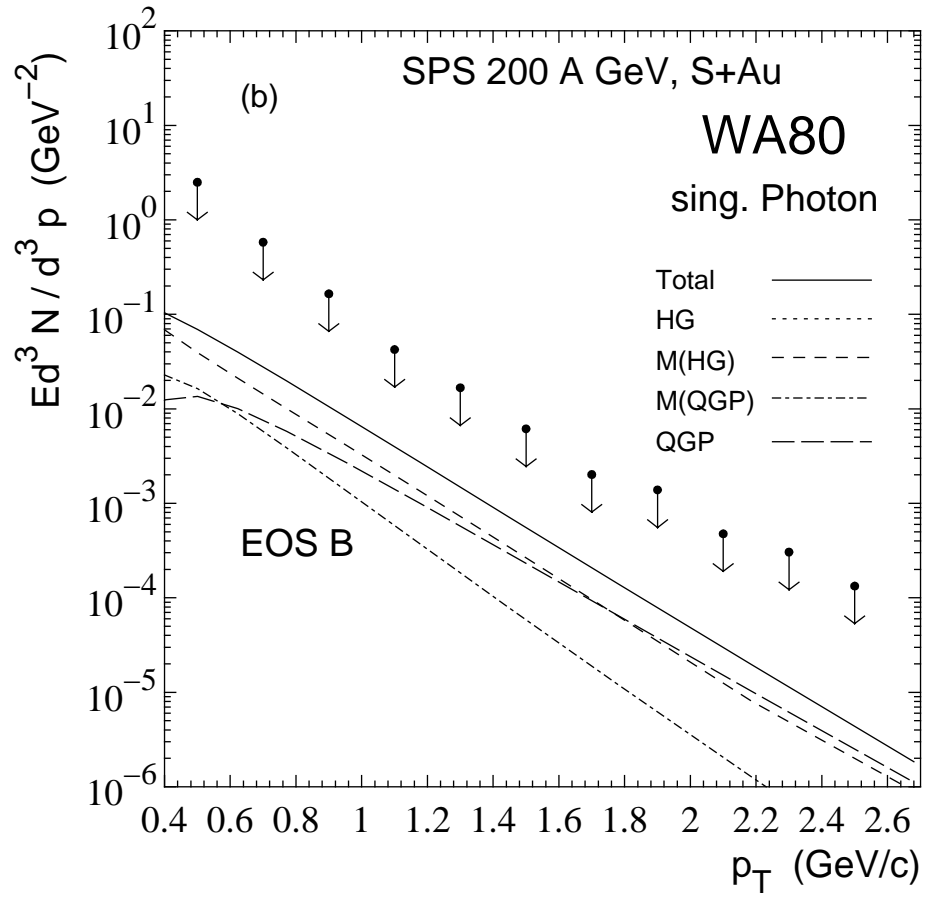


Figure 7b

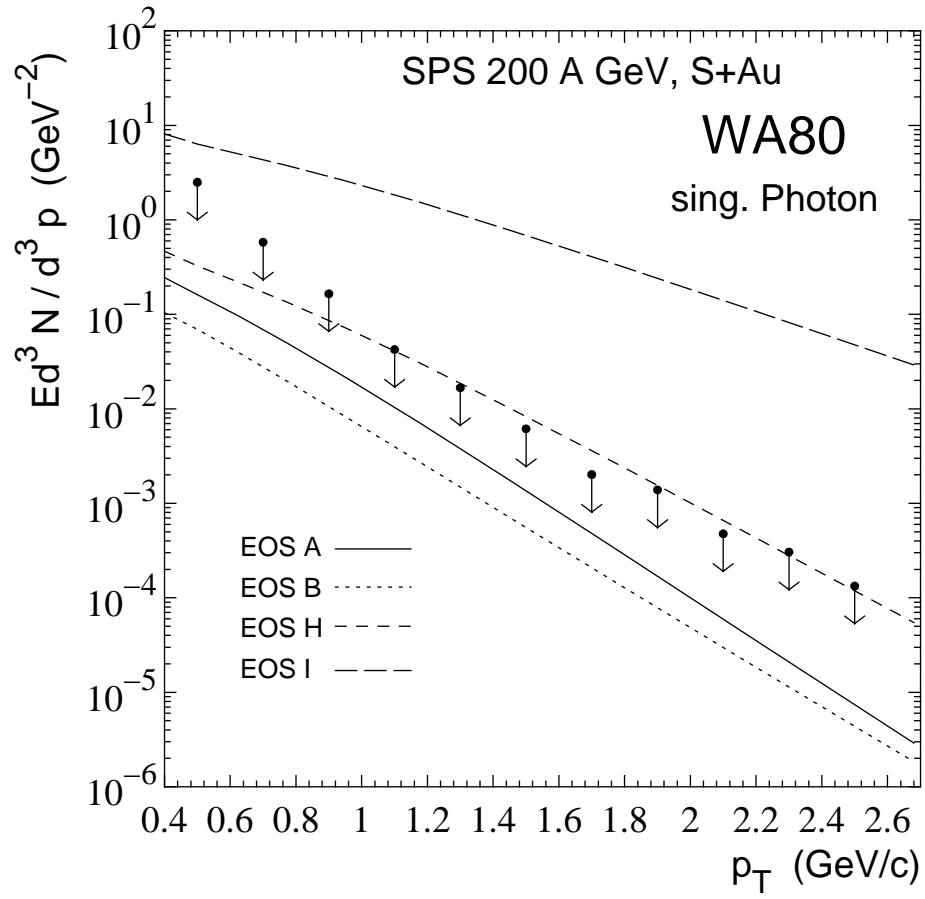


Figure 8

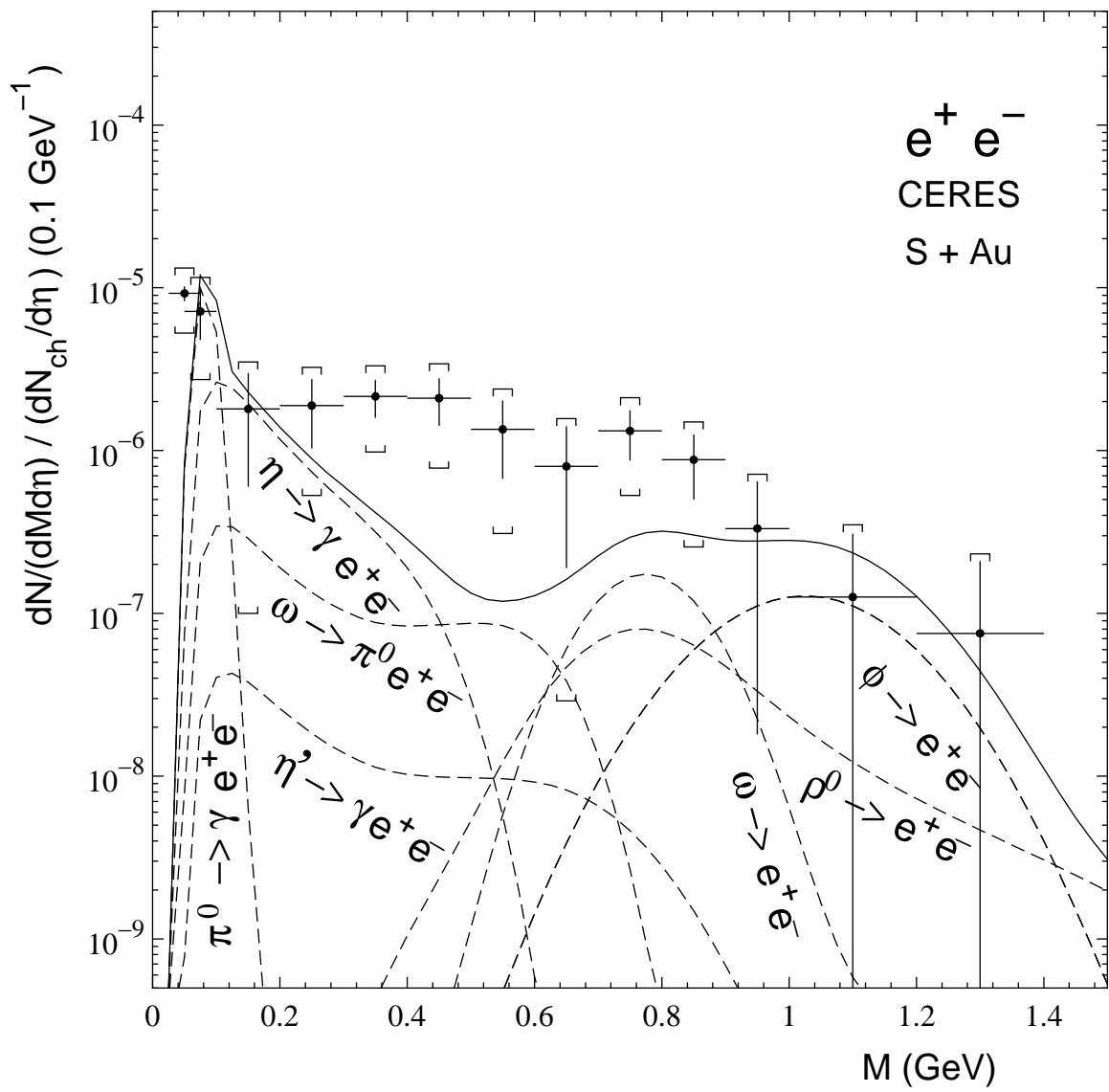


Figure 9

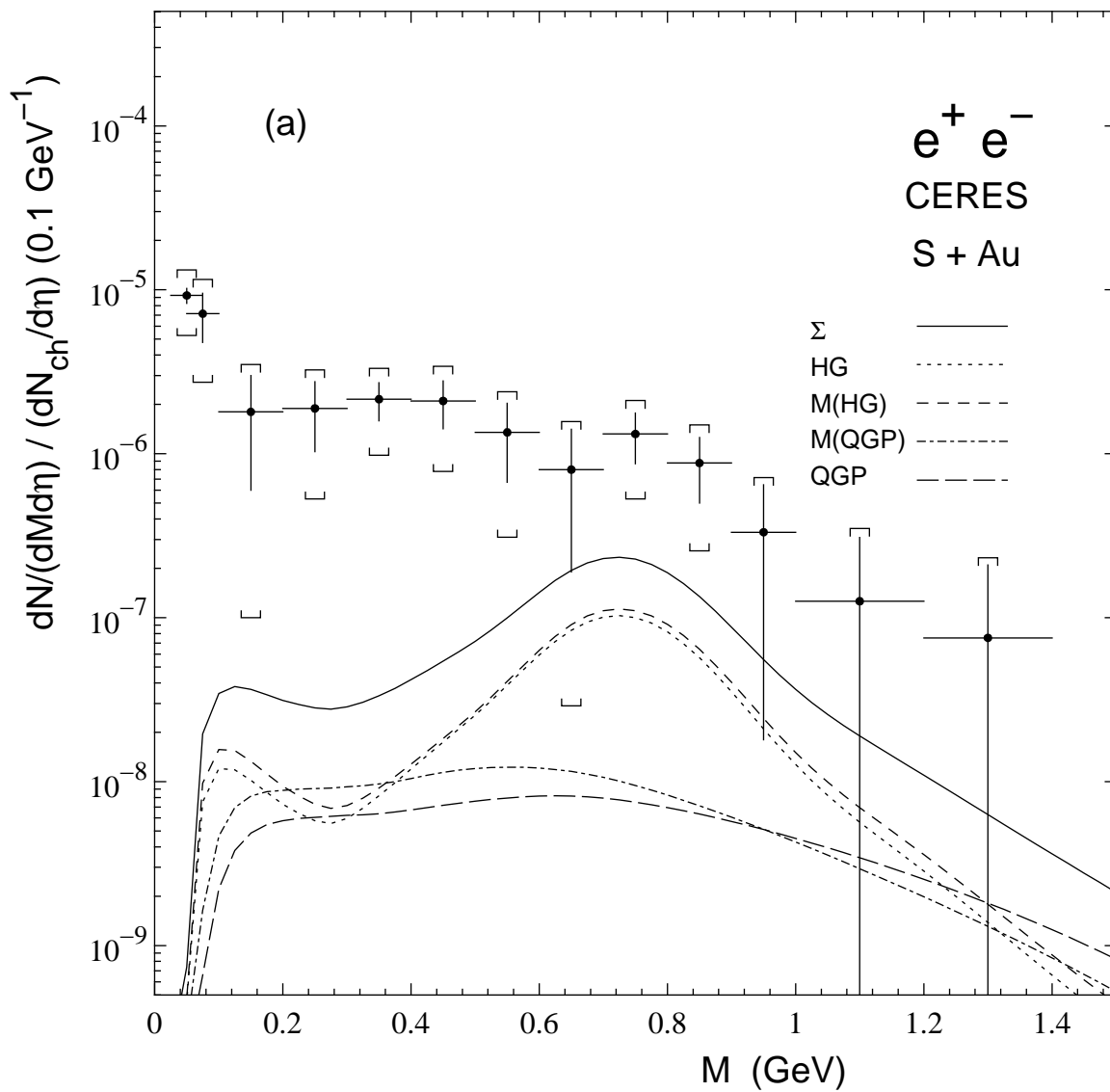


Figure 10 a

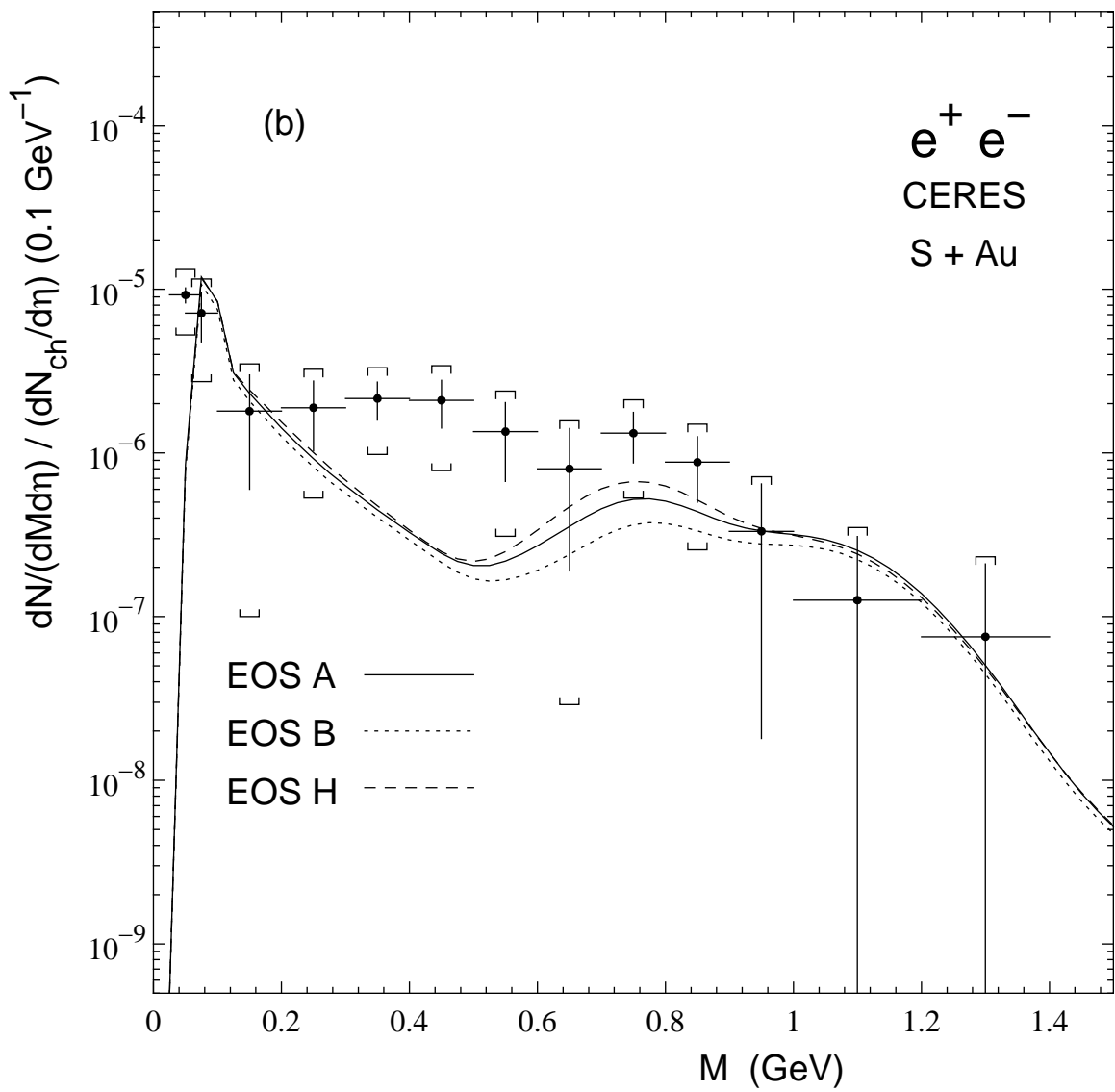


Figure 10 b